Title
Evaluation of alternative designs for an injectable barrier at the Brookhaven National Laboratory Site, Long Island, New York

Journal
Water Resources Research, 35(10)

Author
Moridis, G.

Publication Date
1999

LBNL-41763
Preprint

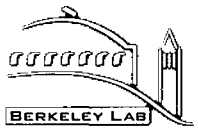

ERNEST ORLANDO LAWRENCE
BERKELEY NATIONAL LABORATORY

Evaluation of Alternative Designs for an Injectable Barrier at the Brookhaven National Laboratory Site, Long Island, New York

George J. Moridis, Stefan Finsterle, and John Heiser

Earth Sciences Division

January 1999

Submitted to
Water Resources Research

DISCLAIMER

LBNL-41763

EVALUATION OF ALTERNATIVE DESIGNS FOR AN INJECTABLE BARRIER AT THE BROOKHAVEN NATIONAL LABORATORY SITE, LONG ISLAND, NEW YORK

George J. Moridis and Stefan Finsterle
Earth Sciences Division
Lawrence Berkeley National Laboratory
Berkeley, CA 94720

John Heiser
Advanced Technology Department
Brookhaven National Laboratory
Upton, NY 11973

January 1999

This work was supported by the U.S. Department of Energy, Office of Environmental Management, Office of Technology Development, Subsurface Contamination Focus Area, under Contract No. DE-AC03-76SF00098.

Evaluation of Alternative Designs for an Injectable Barrier at the Brookhaven National Laboratory Site, Long Island, New York

George J. Moridis and Stefan Finsterle
Earth Sciences Division, Lawrence Berkeley National Laboratory, University of California, Berkeley, California

John Heiser
Advanced Technology Department, Brookhaven National Laboratory, Upton, New York

Abstract. Two alternative designs for the demonstration emplacement of a Viscous Liquid Barrier (VLB) at the Brookhaven National Laboratory (BNL), Long Island, New York, are investigated by means of numerical simulation. The application of the VLB technology at the BNL site involved a surface-modified colloidal silica (CS), which gels upon addition of an appropriate electrolyte. Lance injection was used for the CS barrier emplacement. The lance injections occur in three stages: primary, secondary and tertiary. The geometry of the barrier is based on the wedge model. The first design is based on optimization principles and determines the parameters that maximize uniformity and minimize permeability by minimizing an appropriate objective function while meeting the design criteria. These include a maximum hydraulic conductivity of 10^{-7} cm/s and a minimum thickness of 1 m. The second design aims to meet the same criteria, and reflects standard chemical grouting practices. The combined effects of the key design parameters (i.e., lance spacing, injection location and spacing, gel time, injection rate and volume) on the barrier permeability are studied. The optimization-based design is shown to have a significantly better performance than the standard engineering design. The interpenetration of adjacent CS bulbs appears to be of critical importance in meeting the barrier specifications. The 3-D simulations show that the barrier performance depends heavily on the path by which the final state is achieved. The *in situ* field measurements of the barrier permeability are consistent with, and appear to validate, the model predictions.

1. Introduction

The development of an effective technology for *in situ* contaminant containment is necessitated by the need to prevent further release of contaminants from buried sources and the need to contain existing contaminant plumes. Contaminants can migrate toward previously uncontaminated regions of the subsurface. Excavation and disposal of contaminated soils may pose environmental health and safety problems, is expensive and often impractical.

Subsurface barriers, formed by injection of barrier fluids that gel or solidify *in situ*, can contain contaminants on-site and control the groundwater flow pattern, thus reducing the risk of off-site migration. Containment is also necessary to prevent the spread of mobilized contaminants resulting from application of aggressive treatment technologies (e.g., soil flushing, surfactant treatment) that increase the mobility of the contaminants.

1.1. The VLB Technology Concepts

Lawrence Berkeley National Laboratory (LBNL) staff have developed the Viscous Liquid Barrier (VLB) technology [*Moridis et al.,* 1994;1995;1996a,b,c;1997a,b; *Persoff et al.,* 1994, 1995] for the subsurface isolation of contaminants. VLB employs a new generation of environmentally benign, viscosity-sensitive liquids, the solidification of which is accurately controlled. The low-viscosity barrier liquids are injected into the porous or fractured media of the subsurface through multiple injection points. The plumes merge and completely surround the contaminant source and/or plume. Once in place, they gel or cure to form a nearly impermeable barrier. The technology can also be applied to encapsulate wastes in the subsurface. In applying this technology, however, it is important to match the fluid to the waste and to the soil conditions, and to control the gel time and the emplacement of the fluid [*Persoff et al.,* 1994, 1995; *Moridis et al.*, 1996a,c].

1.2. The VLB Barrier Liquids

VLB uses two general types of barrier liquids [*Moridis et al.*, 1995; 1996a,b,c; *Persoff et al.*, 1994;1995]. The first is Colloidal Silica (CS), an aqueous suspension of silica microspheres (2-100

nm in diameter) in a stabilizing electrolyte. It has excellent durability characteristics, poses no health hazard, is practically unaffected by filtration, and is chemically and biologically inert. The increase in viscosity of the CS following injection is due to a controlled gelation process induced by the presence of an appropriate electrolyte solution, either one of which is added immediately prior to injection at ambient temperatures. The CS has a tendency to interact with the geologic matrix, and therefore, special formulations or techniques are required to minimize or eliminate the impact of such interactions [*Persoff et al.*, 1998;1999].

The second type belongs to the PolySiloXane (PSX) family, and involves vinyl-terminated silanes with dimethyl side groups. PSX is a pure substance, and as such, it is unaffected by filtration. The increase in viscosity in PSX is caused by the cross-linkage of the injected substances after the addition of a catalyst. The cross-linking process is controlled by the quantities of the catalyst, crosslinker, and (occasionally) retardant added to the PSX prior to injection.

1.3. Applications and Advantages

The VLB technology can be applied – permeability permitting – at many sites where hazardous wastes (radionuclides, heavy metals, organics, mixed wastes) have contaminated the subsurface, including catchment ponds, buried tanks and landfills. It can be used (a) to entomb the wastes, (b) to create a *box* to surround and isolate the contaminated area, (c) to seal the permeable aquifer zones, thereby redirecting flow to lower permeability zones and enhancing the effectiveness of conventional pump-and-treat methods, and (d) for surface applications.

VLB is based on permeation, and as such can be applied in regions with permeabilities orders of magnitude lower than those necessary for the application of cementitious or bentonite slurry grouts. It is not affected by filtration, and is free from the *cold joint* problem, i.e., the presence of permeable pathways at the intersection of grout bulbs. It is not limited by depth considerations (as is the case for slurry walls). It permits the complete isolation of the affected area from regional groundwater flow by providing barriers to both horizontal and vertical flow (*walls* and *bottoms*, respectively). It uses low-viscosity liquids (under 0.01 Pa·s), which allow the use of low injection pressures (thus

reducing the risk of soil fracturing) and conventional injection equipment. Site disturbance and human exposure are minimized, as no excavation is required. It is cost competitive, and applicable to the whole spectrum of wastes and a wide variety of sites. It allows more aggressive remediation technologies (e.g., soil washing, alcohol flooding.), or natural degradation and bioremediation to occur without risk of contaminant migration.

Finally, the VLB barrier liquids are chemically and biologically resistant to degradation and have regulatory acceptance. Because of their environmentally benign nature, CS and PSX have received categorical exclusions from EPA/NEPA regulations for application in California (Los Banos site, see next section), South Carolina (Savannah River Site), and New York (BNL site).

2. The Brookhaven Site Field Demonstration

The first small-scale (proof-of-concept) field test of the VLB technology was successfully conducted at a sand and gravel quarry in Los Banos, California, with subsurface conditions similar to those at the Hanford site [*Moridis et al.*, 1995; 1996a,b,c]. Following that, a scaled-up field demonstration was conducted at a clean site at the Brookhaven National Laboratory (BNL), Long Island, New York. The subsurface geology of the BNL site is characterized by a deep unconsolidated sandy formation. This demonstration called for the emplacement of a barrier in the unsaturated zone (which extends from the surface to a depth of 20 m).

Barrier installation took place in August and September 1997. Following the barrier installation, hydraulic, tracer and geophysical methods were employed to verify and evaluate the barrier. The barrier was subsequently excavated, its shape and configuration were examined, and samples were taken for laboratory analyses.

2.1. Functional Requirements, Conceptual Design and Approach

The acceptance criteria for the barrier performance were a maximum target saturated hydraulic conductivity $K_T = 10^{-7}$ cm/s and a minimum thickness of 1 m. Hence, discussions in this paper are in terms of the hydraulic conductivity K^* (in cm/s) of the grouted soil/CS system, although

permeability k (in m^2) is a more appropriate measure of performance because it is a function of the porous medium only. K^* accounts for both porous medium and fluid properties, and is related to the grouted permeability k^* through the equation $K^* \simeq 100\, k^*\, \rho_w\, g/\mu_w$, where ρ_w is the water density (kg/m^3) and μ_w is the water viscosity (Pa· s).

The barrier design called for a half inverted roof or wedge configuration (Figure 1). A detailed description of the barrier, as well as detailed engineering drawings with dimensions and specifications, can be found in *MSE* [1997]. The barrier geometry and basic dimensions are shown in Figure 1, which also depicts the injected bulbs of CS. Lance injection was selected as the barrier emplacement method [*MSE*, 1997]. In the lance injection system used at the Brookhaven site (Figure 2), 3 small-diameter probes (0.045 m OD) are inserted simultaneously into the ground, and liquids are injected through holes located at the lance tip (Figure 3).

The barrier included vertical walls and slanted wells at a a 45 degree angle from the vertical (Figure 1). To ensure the best possible seal between lances and soil (and thus alleviate potential leakage problems), injection occurred while the lance moving downward.

2.2. Soil Properties

The soil properties used in the simulations represent the arithmetic average of laboratory analyses of 6 disturbed samples prepared by compressing loose soil from the BNL subsurface to a density equal to that of the undisturbed soil (1650 kg/m^3). The soil porosity ϕ was 0.38, and its horizontal permeability k_x was 10^{-11} m^2, corresponding to a saturated hydraulic conductivity $K_x = 10^{-2}$ cm/s. The vertical permeability k_z was 1/10th of k_x. In the simulations, $\log k_x$ and $\log k_z$ varied randomly, with a mean of -11 and -12, respectively, and a standard deviation of 1. The capillary pressure P_c vs. water saturation S_w curve of the BNL soil and the fitting curve using the *van Genuchten* [1982] model are shown in Figure 4. The gas and liquid relative permeabilities were obtained from the *van Genuchten* [1980] model and the parameters in Figure 4.

2.3. The Barrier Liquid

The barrier fluid selected for injection at the BNL site was Nyacol DP5880, a CS variant. Nyacol DP5880 has a nominal particle size of 8 nm, a silica content of 30wt%, a pH of 6.5, and is stabilized by a permanent particle charge produced by isomorphic replacement of Si by Al on the particle surface. This type of CS was developed to alleviate adverse soil effects, which could lead to uncontrolled gelling [*Moridis et al.*, 1996c; *Persoff et al.*, 1998]. An aqueous solution of $CaCl_2$ was used to induce gelation.

The experimentally determined time-variable viscosity of the CS-$CaCl_2$ system (Figure 5) was used in the simulations, with appropriate parametric factors for adjustments during optimization (Table 1). The lower limit of the gel time was set to 1 hr, as shorter gel times could be impractical.

2.4. The Alternative Designs

Two alternative designs were proposed. The first design is based on optimization principles and determines the design parameters that maximize uniformity and CS gel saturation in the pore space of the injected zone by minimizing an appropriate objective function while meeting the design criteria. The basic design parameters determined by the optimization are (a) the lance spacing (the distance between lances), (b) the injection spacing (the distance between injection points along the same lance), (c) the injection volume and rate, and (d) the gel time, i.e., the time for CS solidification.

The second design reflects standard engineering practices of grout injection, and involves estimates of design parameters based on previous injection experience. This approach relies empirically on repeated injections (until refusal is attained) to meet the design criteria.

3. The Numerical Models

The two alternative designs were evaluated by means of numerical simulation. The TOUGH2 [*Pruess*, 1991] general-purpose simulator with the EOS11 module [*Finsterle et al.*, 1994] were used for the forward simulations. Optimization simulations were conducted by coupling TOUGH2/EOS11 with the ITOUGH2 inversion code [*Finsterle*, 1997].

3.1. TOUGH2/EOS11 for Forward Simulations

Here we present a short description of the EOS11 module. Detailed descriptions can be found in *Finsterle et al.* [1994, 1997].

3.1.1. Conceptual approach. Injection of CS into a porous medium leads to a system which consists of three separate phases, namely the solid grains, a non-condensable gas (in the unsaturated zone), and an aqueous phase containing CS. During the gelling process, the viscosity increases, turning the gel-water mixture into a non-Newtonian, visco-elastic fluid that eventually solidifies. The appearance of a new phase, i.e., the solidified gel, leads to changes in the physical and chemical properties of the porous medium. At the end of gelation, the resulting new porous medium has a lower porosity, a new pore structure, reduced permeability, and different wettability characteristics.

The following major assumptions are made in EOS11:

(1) The chemical process of gelation is not explicitly modeled. Instead, we model the viscosity of the liquid phase as a function of grout concentration and time. The evolution of viscosity with time is measured in the laboratory and represented by a *gel time curve*. Mixture viscosity varies with the concentration of gel in the aqueous phase, and is described by a *mixing rule*.

(2) The grout is treated as a miscible, aqueous solution. Upon gel solidification, described by the *solidification model*, the resulting new porous medium has lower porosity and permeability, and different wettability characteristics.

(3) The injection and redistribution of CS follows the basic approach of the three-dimensional, multiphase, multicomponent, nonisothermal numerical simulator TOUGH2 [*Pruess*, 1991].

3.1.2. Gel Time Curve and Mixing Rule. In the subsurface, the pore space is occupied by two fluids: the gaseous phase, consisting of air and water vapor, and the liquid phase, which is composed of water, CS, and dissolved air. The viscosity of the liquid phase depends on grout concentration and time. The increase of pure grout viscosity as a function of time is described by the gel time curve, a parameterized function that can be fitted to laboratory data. Based on the

laboratory measurements [*Persoff et al.*, 1998], the gel time curve is described by

$$\mu_{gel} = \gamma_1 + \gamma_2 \exp(\gamma_3\, t)\,, \tag{1}$$

where t is the time (s), and γ_1, γ_2 and γ_3 are fitting parameters. The injected CS is diluted due to mixing with pore water. The mixing rule calculates the viscosity of the liquid phase, μ_ℓ, as a function of t and the gel mass fraction in the liquid phase, X_ℓ^{gel}. The available mixing rules are:

$$\mu_\ell = \begin{cases} X_\ell^{gel}\,\mu_{gel} + (1 - X_\ell^{gel})\,\mu_w & \text{Linear mixing rule} \\ \left(\dfrac{X_\ell^{gel}}{\mu_{gel}} + \dfrac{1 - X_\ell^{gel}}{\mu_w}\right)^{-\frac{1}{b}} & \text{Power-law mixing rule} \end{cases} \tag{2}$$

3.1.3. The Solidification model. The solidification model is based on the assumption that all of the liquid in the pore space eventually solidifies if the grout in the liquid phase exceeds a certain minimum concentration, X_{min}^{gel}. We introduce a parameter A as follows:

$$A = \begin{cases} 1 & \text{for } X_\ell^{gel} \geq X_{min}^{gel} \\ \dfrac{X_\ell^{gel}}{X_{min}^{gel}} & \text{for } X_\ell^{gel} < X_{min}^{gel} \end{cases} \tag{3}$$

For example, a $X_{min}^{gel} = 0.05$ means that all the liquid with $X_\ell^{gel} \geq 0.05$ eventually solidifies. The fluid with lower gel concentrations solidifies incompletely.

The liquid saturation, S_ℓ, at the time solidification occurs is denoted by S_ℓ^{sol}. All soil characteristics and initial conditions referring to the new porous medium are denoted by a star (*). The porosity of the grouted medium is reduced by the amount of gel that solidifies, i.e.,

$$\phi^* = \phi\,(1 - A\,S_\ell^{sol})\,. \tag{4}$$

The porosity reduction leads to a decrease in the permeability k. The partial clogging of the pore space by grout is conceptually similar to the permeability reduction due to phase interferences in a multiphase flow system. The *Permeability Reduction Model* describes the permeability reduction as

$$k^* = k \cdot F\,, \tag{5}$$

where F is the permeability reduction factor described by various models as

$$F = \begin{cases} k_{rg} = k_r(S_g) & \text{Relative permeability model} \\ (1 - A\,S_\ell)^\beta & \text{Power law model [\textit{Todd}, 1990]} \\ \dfrac{(1 - A\,S_\ell)^3}{(A\,S_\ell)^2} & \text{Blake-Cozeny-Carman model [\textit{Oldenburg and Spera}, 1992]}, \end{cases} \tag{6}$$

where k_{rg} is value of the gas relative permeability k_r evaluated at $S_g = 1 - A\,S_\ell^{sol}$ is the gas phase saturation, and β is a fitting parameter.

Due to the reduced pore sizes, the capillary pressure of the grouted soil is expected to be more negative for a given water content, and is calculated by *Leverett*'s [1941] scaling rule as:

$$P_c^*(S_\ell^*) = P_c(S_\ell^o)\sqrt{\frac{k\,\phi^*}{k^*\,\phi}} \tag{7}$$

where S_ℓ^* is the liquid saturation in the (grouted) new porous medium, and

$$S_\ell^o = A\,S_\ell^{sol} + S_\ell^* \left(\frac{\phi^*}{\phi}\right) = A\,S_\ell^{sol} + S_\ell^*\,(1 - A\,S_\ell)\,. \tag{8}$$

Given a certain liquid saturation of the grouted soil, (8) provides the original liquid satura-tion corresponding to the same water content. The capillary pressure is then obtained and rescaled by applying (7). Finally, the liquid saturation after solidification is calculated as the volume of the ungelled pore fluid divided by the porosity of the new medium. Note that the solidification model has to be applied to each grid block of the discretized flow region to provide initial conditions and soil properties of the grouted medium for subsequent simulations.

3.2. ITOUGH2 for Inverse Modeling

The optimization of operational parameters affecting barrier emplacement is performed using ITOUGH2 *Finsterle* [1997]. The main purpose of ITOUGH2 is to estimate hydrogeologic parameters by automatically calibrating a TOUGH2 model against laboratory or field data. In ITOUGH2 inverse modeling, an objective function measuring the misfit between the observed

and calculated system response is iteratively reduced using nonlinear minimization (Levenberg-Marquardt algorithm and simulated annealing) in the multidimensional parameter space.

The same approach can be used to optimize the barrier injection design. The objective function is composed of three components corresponding to (a) the K^* magnitude, (b) the uniformity of K^* distribution, and (c) the minimum barrier thickness, and assigns very large penalty terms if the design criteria are not met. The operational parameters (see Table 1), which are input parameters to the simulator, are then determined such that they minimize the composite objective function while meeting the design criteria. Numerous examples of ITOUGH2 inversions to determine hydrologic parameters in strongly nonlinear systems can be found in the literature, e.g., *Finsterle and Persoff* [1997], *Finsterle and Najita* [1998], *Finsterle and Faybishenko* [1999]. Details about the minimization algorithm will not be discussed here, but can be found in *Finsterle* [1997].

4. The Optimization-Based Design (OBD)

4.1. Conceptual Design

To ensure high uniformity and sealing of the pore space, injections proceed in three stages in the OBD. The first stage, called the primary, follows the outer perimeter of the proposed barrier walls, creates the boundary skeleton or foundation, and results in the low-permeability core which constitutes the bulk of the barrier. Primary injections are followed by secondary injections, which proceed above the primary injections along the inner perimeter of the proposed barrier, and aim to fill and seal imperfections in the primary barrier. The primary and secondary injections and their relative locations are shown in Figure 1.

Injections in the third, tertiary stage occur at the centers of the grid defined by the primary and secondary injections, involve limited volumes and may not even be necessary. They are intended to seal the few small pockets that may have been bypassed due to heterogeneities in the matrix. The optimization process described in the following section determined that, in the OBD, the primary is the main injection, while the secondary and tertiary injections are auxiliary in nature.

4.2. Simulation Approach

In the development of the OBD, the objective function discussed in Section 3.2 was complemented with a constraint on the maximum injection pressure, which was not allowed to exceed 1.5 times the lithostatic in primary injections to avoid possible soil fracturing. It was possible to optimize the design by (a) maximizing the barrier performance for a given quantity of CS, or (b) by minimizing a cost function associated with the CS injection volumes and the labor costs. However, because of the importance of this first medium-scale application, the OBD was based on the maximization of barrier performance regardless of any other consideration.

From the first few optimization iterations, it was evident that the optimum design parameters for the slanted injections invariably optimized the vertical injections, which resulted in a system with a lower K^* with more uniform distribution. In light of this fact and the significant execution times, only optimization simulations for the slanted system were conducted.

4.3. OBD Domain Discretization and Data Inputs

The parameters used in the simulation are shown in Table 1, which also includes the initial values of the parameters to be optimized (denoted by an asterisk). In EOS11 [*Finsterle et al.*, 1994] the default gel time is 1 hr, and in the simulations it is multiplied by a scaling factor (see Table 1) to provide the actual gel time. Figure 6 shows the (x, y) grid used both in the vertical and slanted simulations. The thick line in Figure 6 defines the simulation stencil, i.e., the basic symmetry element in the injection process, which was the simulation domain in the (x, y) plane.

Figure 7 shows the (x, z) grid in the slanted simulations. Only the active grids are shown in Figures 6 and 7, i.e., the boundaries are not shown. The active domain consisted of 7308 gridblocks $(28 \times 9 \times 29)$ in (x, y, z) and 21924 equations. The initial grid spacing was $\Delta x = \Delta y = \Delta z = 0.15$ m. ITOUGH2 determined $\Delta\ell_1$ and $\Delta\ell_2$, which define the optimized $\Delta y = \Delta\ell_1$ and $\Delta x = \Delta z = \Delta\ell_2$. The $\Delta\ell_1$ and $\Delta\ell_2$ optimizations determined the lance and injection spacings, respectively.

The groundwater level was at $z = -18$ m, and the initial water saturation distribution was

computed from the watertable elevation and the P_c function (Figure 4). Boundary cells with constant pressure (101.3 kPa, i.e., atmospheric pressure) and saturation (equal to the initial S_w) were located at the two boundaries $x = 0$ and $x = x_{max}$. An atmospheric boundary cell with $P_c = 0$ was located at the top of the domain, allowing air to escape but preventing water movement into it. These boundary gridblocks are not shown in Figures 6 and 7. Because of symmetry, no-flow boundaries were specified at $y = 0$ and $y = y_{max}$.

The circles in Figures 6 and 7 are the projections of the spherical bulbs onto the (x, y) and (x, z) planes, respectively. During the primary injections, CS is first injected at location P1 on the primary axis (Figure 7), and then at the lower location P2 as the lance moves downward. Due to the three-dimensional nature of this system, the distances involved are not obvious, but can be computed using principles of stereometry.

Figure 8 shows all the relevant quantities and their relationships for an isotropic system. Note that in our analysis the porous medium was anisotropic, and the quantities in Figure 8 were used as initial values in the optimization. For maximum uniformity between primary injections, the principles of stereometry dictate that the lance spacing be equal to the injection spacing (i.e., [CB] = [CG] = a) and equal to the distance between the axis of primary and secondary injections (i.e., [AF] = e = a). This occurs when the angle $\theta = 67.8^o$, corresponding to a surface distance

$$[AD] = c = (a/2)\tan\theta$$

in the isosceles triangle ABC, and c = 1.84 m for the initial a = 1.5 m. For maximum uniformity between primary and secondary injections, the secondary injection point must be located at the intersection of the plane perpendicular to both the primary and secondary axes and passing through the midpoint of CG. The offset g (as well as the corresponding vertical difference) is then easily computed from the relationship shown in Figure 7.

The tentative locations of the secondary injection points in the nonisotropic systems were initially those determined from Figure 8 (point H). We then identified the gridblock along the AH axis into which injection was possible (after the solidification of the primary injection) without

exceeding the maximum pressure constraints. The search algorithm focused on 7 gridblocks along the secondary injection axis AH, i.e., the injection gridblock and 3 gridblocks above and below the injection point. If the maximum pressure constraint was violated at all seven gridblocks on the AH axis, the search moved to the axis parallel to and immediately above to the AH axis.

Finally, a skin factor was applied to all gridblocks along the injection axis. The skin permeability was $k_{skin} = k/10$, and applied to all directions.

4.4. OBD-Parameters for Maximum Barrier Performance

The optimized parameters are shown in Table 2. In the OBD, a total of 46 optimization iterations were needed for the determination of the design parameters that minimized the objective function. These design parameters were (a) $\Delta\ell_1$, from which the the lance spacing was determined as $L_1 = 8\Delta\ell_1$, (b) $\Delta\ell_2$, from which the injection spacing was determined as $L_2 = \Delta\ell_2\sqrt{2}$, (c) the injection mass M, (d) the injection rate Q, and (e) the gel time scaling factor.

Larger grid spacings resulted in unacceptable levels of K^* and heterogeneity, which could not be overcome by subsequent injections. Injection of the correspondingly larger volumes within the limited time allowed by the gel time required unacceptably high pressures (20-30 times the atmospheric) to avoid gelation of the advancing CS front and impedance to further liquid movement. Longer gel times allowed more time for liquid CS redistribution, and, coupled with heterogeneity, caused very poor gel uniformity and unacceptably high K^*.

The design parameters in Table 2 result in a substantial overlap (i.e., interpenetration) of adjacent bulbs. Assuming idealized conditions (i.e., bulbs which are perfect spheres), the overlap is about 30% of the distance between the centers of the bulbs (Figures 6 and 7). This substantial interpenetration is capable of overcoming the problem of bulb deformation (due to gravity and heterogeneity), which could adversely affect the barrier performance.

4.5. OBD Primary Injections

CS was injected at two points: first at $x = 1.85$ m, $y = 0.45$ m and $z = -0.75$ m, and then

at a lower elevation at $x = 1.15$ m, $y = 0.45$ m and $z = -1.75$ m (Figure 7). Contour plots of the final porosity ϕ^* and saturated hydraulic conductivity K^* were obtained on three different y planes: the Y_0, Y_1 and Y_2 planes of the centers of the $(i, j = 5, k)$, $(i, j = 3, k)$ and $(i, j = 1, k)$ cells in (x,y,z), respectively (Figure 6). The Y_2 plane is that of maximum expected heterogeneity. The Y_1 plane represents a mid-point between the boundary Y_2 plane and the injection plane Y_0.

The ϕ^* distribution after redistribution and solidification of the primary injections on the Y_0 plane is shown in Figures 9, which shows a flattening of the CS bulb. This is due to the soil anisotropy introduced by the 1:10 vertical to horizontal permeability ratio. The ϕ^* distributions on the Y_1 and Y_2 planes are practically identical and are not shown. There is as substantial reduction in ϕ in the majority of the target space to values smaller than 0.01 from the original $\phi = 0.38$. The compression and sagging of the contour lines above and below the combined bulbs conform to expected redistribution patterns due to gravity. The substantial ϕ reduction is attributed to the large injection volumes, which allow the removal of pore air through displacement by the advancing CS, diffusion through, and solution into the liquid phase.

The $\log K^*$ distribution on the Y_0 plane is shown in Figure 10. The permeability of the majority of the target space is lowered to the $\log K^* = -10.5$ level (corresponding to $K^* = 3.16 \times 10^{-10}$ cm/s) from the original level of $K = 10^{-2}$ cm/s). The deviation of the $\log K^*$ on the Y_2 plane from the one on the Y_0 plane is shown in Figure 11, in which the zone of near-zero deviations > 1 m and covers practically all of the grouted region. The very low values of the deviations and their very localized nature (which preclude the use of a contour plot in Figure 11) demonstrate the effectiveness and uniformity of the CS application and confirm the validity of the OBD.

Inspection of Figures 9 through 11 demonstrates that the weakest link in the grouted system is the *throat* (i.e., the constriction) between the two bulbs. Achieving a uniform low permeability of this region is the primary objective of the barrier emplacement effort, since this is the likely location of leaks. The $\log K^*$ distribution on the Z_0 plane – at $(i, j, k = 13)$ in (x, y, z), passing by the throat – in Figure 12 shows a barrier (delineated by the zone with $\log K^* \leq -7$) with a thickness meeting

the 1 m design criterion. Thus, the weakest point in the grouted system meets the design criteria. The implication of these observations is that, in the OBD, the functional requirements of the barrier are met after the primary injection.

4.6. OBD Secondary Injections

Based on the results of the primary injections, it appears that secondary injections are not necessary. However, field realities require secondary injections to correct possible imperfections.

Following the discussion in Section 4.3, the distance between the primary and secondary injection lines at the surface, i.e., the distance c in Figure 8, is $c = \frac{\alpha}{2}\tan\theta = \frac{0.9}{2}\tan(67.8^o) = 1.1$ m.

It would be desirable to conduct the secondary injections while the CS from the primary injections was still liquid, as preliminary simulations had shown that this resulted in maximum permeability reduction by avoiding stagnation problems. However, the depth of the proposed barrier precluded this possibility, as (a) either high injection rates and high injection pressures (well in excess of the lithostatic) or (b) impractically long gel times would be required. Therefore, the primary injections are expected to have solidified at the time of the secondary injections. This significantly increased the execution times because of the extreme heterogeneity of the solidified system, each gridblock of which had different porosity and wettability characteristics.

The locations of the secondary injections were determined (Section 4.3) at the gridblocks (a) $i = 6$, $j = 1$ and $k = 13$, and (b) $i = 6$, $j = 9$ and $k = 13$, i.e., they are in the immediate vicinity of the throat. Only 100 kg (1/4th of the primary injection mass) of a CS/electrolyte system with a gel time of 1.8 hrs were injected. The $\log K^*$ contour plot in Figure 13 shows that the secondary injection eliminates the throat, and further expands the zone in which $K^* \leq 10^{-7}$ cm/s.

5. The Standard Engineering Design (SED)

5.1. SED Concepts and Design Parameters

The SED, which was adopted by the contractor at the BNL site barrier [*MSE*, 1997], does not involve parameter estimation based on optimization principles but rather on standard empirical

practices. Primary and secondary injections carry approximately the same weight, and the voids left between them are expected to be sealed by the tertiary injections. In field applications, the SED involves primary and secondary injections of given volumes, and tertiary injections until refusal.

5.2. SED Simulation Domain and Input Data

Simulations of the flow and behavior of the CS were conducted on the stencil (smallest repeatable element) of the SED design. Figure 14 shows the grid spacing on the (x, y) plane, as well as the locations of the primary, secondary and tertiary injections. The circles shown in Figure 14 mark the projection of the spherical CS-grouted bulbs on the corresponding planes. Figure 15 shows the (x, z) grid. Only the active grids are shown in Figures 14 and 15.

The operational parameters of the SED during the barrier installation in August and September 1997 are provided in Table 3 [*MSE*, 1997]. The boundary conditions were the same as in the OBD. This fine resolution allowed the study of localized phenomena and processes and provided an accurate description of sharp interfaces. The domain discretization resulted in 8316 active gridblocks ($36 \times 7 \times 33$) in (x, y, z), which resulted in a total of 24948 equations. This discretization is considerably finer than the one used in the OBD design, but was deemed necessary due to the smaller injection volumes.

5.3. SED Primary Injections

CS was injected at two points: first at $x = 0.525$ m, $y = 0.0025$ m and $z = -1.025$ m, and then at a lower elevation at $x = 0.925$ m, $y = 0.0025$ m and $z = -1.425$ m (Figure 15, points P1 and P2, respectively). Contour plots of ϕ^* and K^* after solidification were obtained on three different y planes: the Y_0 plane at $y = 0.0025$ m, the Y_1 plane at $y = 0.175$ m, and the Y_2 plane at $y = 0.3475$ m. The Y_2 plane is that of maximum expected heterogeneity and is closest to the no-flow boundary at $y = y_{max}$. The Y_1 plane represents a mid-point between the boundary Y_2 plane and the injection Y_0 plane.

Review of the ϕ^* distribution after solidification on the Y_0 and Y_2 planes (Figures 16 and 17,

respectively) reveals the flattening of the CS-grouted bulbs (due to the soil anisotropy) observed in the OBD design. The anisotropy improves the uniformity on the (x, y) plane, but affects adversely uniformity on the (x, z) and (y, z) planes because it limits the vertical distribution of CS. This can have a serious impact in the ability to seal the space between the bulbs.

The lowest ϕ^* with the most uniform distribution over the largest area is observed on the Y_0 plane. On the Y_2 plane, ϕ^* is generally higher and there is a significantly smaller area with $\phi^* \leq 0.04$. Had the soil been isotropic, the SED would result in an interpenetration of about 0.01 m at the boundary, which is insufficient to effect the desired coverage and degree of uniformity. Additionally, such limited interpenetration does not account for field realities (such as lance drifting and heterogeneities), which could adversely affect barrier emplacement and performance.

In the majority of the grouted soil, $\phi^* > 0.1$ and $\min(\phi^*) = 0.04$ at the injection gridblocks. The minimum ϕ^* values are about an order of magnitude larger than those for the OBD. The difference is due to the limited injection volumes. The effect of the insufficient interpenetration of the injected CS bulbs is evident. The ϕ^* distribution on the Y_0 and Y_2 planes demonstrates a gap between the first and second primary injected bulbs, which is virtually unaffected by the CS injection. This space is centered about the $z = -1.225$ m plane (hereafter referred to as the Z_0 plane) and defines the throat of the bulb connections which has been shown to represent the weak link and the most likely location where barrier specifications would not be met. The bulb interpenetration improves with the proximity to the injection point (moving from the Y_2 to the Y_0 planes), but only marginally. At no point do we observe a merging of the cores of the two bulbs.

Figure 18 shows the Y_0-plane distribution of the $\Delta\log(K^*)$, which describes the deviation of K^* (in cm/s) from the target of $K_T = 10^{-7}$ cm/s, and is defined as

$$\Delta\log(K^*) = \log K^* - K_T = \log K^* - 7\,. \tag{9}$$

Negative $\Delta\log(K^*)$ values indicate K^* higher than the K_T. For ungrouted BNL soil, $\Delta\log(K^*) = -5$. The $\Delta\log(K^*)$ distributions on the Y_2 plane is shown in Figure 19. From Figures 18 and 19, it is obvious that, after the primary injections, the K^* distribution substantially exceeds the K_T

target everywhere. Even at the centers of the injected bulbs, K^* is about 2 orders of magnitude higher than K_T, and $\min\{\Delta\log(K^*)\} = -1.69$. This value does not meet the K_T criterion, but is sufficiently low to prevent secondary injection at these points.

Of particular interest is the $\Delta\log(K^*)$ distribution on the Z_0 plane (i.e., the throat of the bulb connection) in Figure 20, where K^* is at best 3.8 orders of magnitude larger than K_T and indicates that this area is very little affected by the CS injection. This is attributed to the inadequate CS injection volumes, which result in very limited interpenetration of the CS-grouted bulbs.

These results indicate that, at the end of the primary injections, the limited interpenetration of the grout bulbs leads to a honeycombed, extremely non-uniform, and unacceptably high K^* distribution. Consecutive injections along the same lance axis during the primary injection cannot adequately fill the pore space because of the limited CS injection volumes and the soil anisotropy. The picture that evolves after the end of the primary injection is that of a set of flattened CS-grouted bulbs centered on a regular grid, which at no point meet the K_T specification and are separated in the vertical direction by a practically undisturbed soil zone.

5.4. SED Secondary Injections

In the secondary injections in the SED design, the injection volumes, injection rates, and the gel time of the CS were the same as in the primary injection. The distributions of the hydraulic properties of the grouted soil at the end of the primary injections were extremely heterogeneous. This resulted in an increase in the execution time by a factor of about 12 over the primary simulations.

The secondary injection is at $x = 1.275$ m, $y = 0.3475$ m and $z = -1.025$ m (Figure 14). Figure 21 shows the residual ϕ^* after the solidification of the secondary injections on the Y_0 planes (i.e., the plane of maximum expected homogeneity). An interesting observation is that the lowest ϕ^* values are not at the secondary injection point, but rather at the confluence of the primary and secondary bulbs. The ϕ^* distribution in the secondary bulbs is quite similar to that in the primary ones, with $\phi^* = 0.04$ at the injection gridblocks. The ϕ^* distribution on the Y_2 plane is similar, but

has generally higher values. At the throat, max(ϕ^*) = 0.24 on the Y_2 plane, larger than the max(ϕ^*) = 0.18 on the Y_0 plane. Such large ϕ^* in this area indicates very limited penetration by CS and a high permeability pathway between the less permeable bulbs.

The $\Delta\log(K^*)$ distribution on the Y_0 plane (Figure 22) follows the pattern of ϕ^*. An area of limited extent at the confluence of the primary and secondary bulbs meets the K_T criterion. The remaining portion of the secondary bulb, however, has an unacceptably high level of K^* which follows a pattern similar to that in the primary injections. Of particular importance is the area about the Z_0 plane. The contour plot of $\Delta\log(K^*)$ on the Z_0 plane in Figure 23 shows very little improvement over the one at the end of the primary injections (Figure 20).

Despite the fact that CS is free of the cold-joint problem, the secondary injections are unable to effect a substantial areal decrease in permeability due to the soil properties after the solidification of the primary injections. The gelation of the primary CS injections creates a new soil matrix adverse to the potential success of further injections because of locally decreased permeabilities. The K^* of the solidified soil/CS system is sufficiently low (at least locally) to prevent adequate CS penetration, but fails to meet the barrier specifications. The problem is exacerbated by stagnation during the secondary injections, which does not allow sufficient coverage of the space between bulbs.

After the solidification of the secondary injections, the final product is two rows of flattened CS bulbs which meet the K_T criterion only in small localized zones at the intersections of the primary and secondary CS bulbs. The majority of the CS-grouted volume has a K^* that is sufficiently low to render it impermeable to CS penetration but fails to meet the target K_T. The rows of flattened bulbs are separated vertically by high-permeability zones of soil with limited CS coverage. The overall system performance does not meet the barrier specifications.

5.5. SED Tertiary Injections

The tertiary injection points T1 and T2 are located at $x = 1.275$ m, $y = 0.0025$ m and $z = -1.225$ m, and $x = 0.925$ m, $y = 0.3475$ m and $z = -1.225$ m, respectively (Figure 14).

Figures 24 and 25 show the $\Delta\log(K^*)$ distribution on the Y_0 and Z_0 planes after the solidification of the tertiary injections at the T1 and T2 points (Figure 15). It is evident that tertiary injections, if technically feasible, are capable of decreasing K^* to the 10^{-7} cm/s target.

The technical feasibility, however, of tertiary injections, is very much in doubt. To achieve the results in Figures 24 and 25, the injection rate and volume were reduced to half of those in the secondary injections, while the gel time was doubled. Even with the reduced injection rate, the injection pressure at T1 was about 50 times atmospheric pressure (Figure 26), and an order of magnitude larger than that for the primary injection at point P1. Such high pressures are likely to cause soil fracturing, an unwanted consequence as it may lead to an unpredictable CS distribution.

These results lead to the conclusion that it is unlikely that tertiary injections would be possible without fracturing, leakage to the surface along the lance axis, or impractically low injection rates. Secondary injections reach the limit of technically feasible injections, whereas tertiary injections are not expected to improve the barrier performance significantly, if at all. When tertiary injections in the field are not characterized by excessive pressures or very low injection rates, they are likely to correct large-scale imperfections of the primary and the secondary injections rather than being true tertiary injections as defined in this section. Such imperfections could be caused by the presence of heterogeneous strata in the subsurface or by lance drifting, i.e., deviation from its intended axis due to flexing or after encountering pebbles or rocks.

6. Comparison of Predictions to Field Measurements

After the installation of the barrier, *in situ* measurements of K^* were made with Guelph permeameters at a number of points and at different depths within the expected boundaries of the barrier walls. The data were collected by the third author of this paper and by *MSE* [1999], and appear in Table 4, where the well name N_w, the measurement depth D, and K^* are listed.

A review of the *in situ* measurements of K^* shows that they are consistent with the numerical predictions of the secondary injections of the SED (the design employed in the barrier installation),

and appear to validate the numerical model. Note that the very high K^* levels at wells 2-2 and 2-4 at a depth of 2.7 m indicate that the measurements were made outside the expected boundaries of the grouted area, and reflect a K on the same order of magnitude with that at the background (ungrouted) level in wells B-1 and B-2.

7. Summary and Conclusions

Two alternative designs for the demonstration emplacement of a Viscous Liquid Barrier (VLB) in the unsaturated zone of the Brookhaven National Laboratory (BNL) site, Long Island, New York, were investigated by means of numerical simulation. The VLB technology [*Moridis et al.*, 1995a] uses a new generation of environmentally benign barrier liquids which solidify within a predetermined time to contain contamination in the subsurface. A surface-modified colloidal silica (CS), which gels upon addition of an appropriate electrolyte, was selected for the BNL application. The functional requirements for the BNL barrier were a maximum hydraulic conductivity of $K_T = 10^{-7}$ cm/sec and a minimum thickness of 1 m.

Lance injection was selected for the CS barrier emplacement. The lance injections proceeded on a regular grid and occur in three stages: primary, secondary and tertiary. The geometry of the barrier is based on the *inverted-roof* model, and includes vertical walls and walls at a 45-degree angle from the vertical.

Two alternative designs were proposed. The first design is based on optimization principles and determines the design parameters which maximize uniformity and minimize the permeability K^* in the injected zones. The basic design parameters determined by the optimization are (a) the lance spacing (i.e., distance between lances), (b) the injection spacing (between injections points along the same lance), (c) the injection volume and rate, and (d) the gel time, i.e., the time for CS solidification. The second design, which was implemented in the field, reflects standard engineering practices of grout injection, and involves empirical estimates of design parameters.

The two alternative designs were evaluated by means of numerical simulation. The

TOUGH2 [Pruess, 1991] general-purpose simulator with the EOS11 module [*Finsterle et al.*, 1995] were used for the forward simulations. Optimization simulations were conducted by coupling TOUGH2/EOS11 with the ITOUGH2 inversion code [*Finsterle*, 1997]. Using laboratory-derived soil and CS gelling data, the effects of the design parameters on the magnitude and distribution of K^* after the injections were studied. Porosity and permeability contour plots at appropriate cross-sections are used to evaluate the two design approaches.

In the optimization-based design (OBD), the functional requirements of the barrier are met after the primary injection. The OBD design parameters result in a substantial interpenetration of adjacent bulbs of injected CS. This interpenetration is capable of overcoming the problem of bulb deformation (due to gravity and heterogeneity), which could adversely affect the barrier performance because of incomplete coverage of the target zone. Secondary injections further improve the barrier performance. Although they appear unnecessary, they are probably important under field conditions to alleviate imperfections of the primary injections.

In the standard engineering design (SED), the picture that evolves after the primary injections is that of a set of flattened CS-grouted bulbs centered on a regular grid, which at no point meet the barrier specification of final K^* and are separated in the vertical direction by a practically undisturbed soil zone. This is due to the limited injection volumes and the soil anisotropy, and results in limited interpenetration of the grout bulbs in the vertical direction and a honeycombed (extremely non-uniform) permeability distribution of unacceptably high magnitude.

Despite the fact that CS is free of the cold-joint problem, the secondary and tertiary injections in the SED are unable to meet the barrier specifications. This is because the CS solidification creates a new soil matrix, which is adverse to the success of further injections because of permeabilities that are sufficiently low to prevent adequate CS penetration, but are too high to meet the barrier specifications. The solidification of the secondary injections results in a set of rows of flattened CS bulbs which meet the K_T criterion only in small localized zones at the intersections of the primary and secondary CS bulbs, but the majority of the CS-grouted area fails to meet the criterion. The

rows of flattened bulbs are separated vertically by high-permeability zones of limited CS coverage.

Tertiary injections in the SED are shown to be effective in attaining the barrier specifications, but are not deemed technically feasible because of excessively high injection pressures (sufficiently large to induce soil fracturing) or impractically low injection rates. Therefore, secondary injections represent the limit of what is technically feasible, whereas tertiary injections are not expected to improve the barrier performance significantly, if at all. A comparison of the *in situ* measurements of K^* to the numerical predictions of the secondary injections of the SED shows that the two are consistent, and appears to validate the numerical model.

A number of conclusions can be drawn from these results. The OBD is shown to be technically easier and to have significantly better performance than the SED. The traditional SED approach of injection to refusal appears incapable of producing barriers of acceptable performance because the primary and secondary injections create a soil matrix which is not conducive to the success of further injections because of lower permeability, but which is still higher than the target K_T. A very important observation is that the barrier performance depends heavily on the path by which the final state is achieved. Thus, an inappropriate design may not allow corrective action to meet the barrier specifications because of injection pressure and gel time limitations.

Acknowledgments. This work was supported by the U.S. Department of Energy, Office of Environmental Management, Office of Technology Development, Subsurface Contamination Focus Area, under Contract No. DE-AC03-76SF00098. John Apps and Curt Oldenburg are thanked for their insightful review comments. Special thanks are extended to MSE Technology Applications for making available a large portion of the field measurements reported in the paper.

References

Finsterle, S., and B. Faybishenko, Inverse modeling of a radial multistep outflow experiment for determining unsaturated hydraulic properties, *Adv. in Water Resour.*, *22*(5), 431-444, 1999.

Finsterle, S., and J. Najita, Robust estimation of hydrogeologic model parameters, *Water Resour. Res., 34*(11), 2939-2947, 1998.

Finsterle, S., ITOUGH2 Command Reference, *Report LBNL-40041*, Lawrence Berkeley Laboratory, Berkeley, CA, 1997 (on the web at URL http://www-esd.lbl.gov/ITOUGH2).

Finsterle, S., and P. Persoff, Determining permeability of tight rock samples using inverse modelin, *Water Resour. Res., 33*(8), 1803-1811, 1997.

Finsterle, S., C.M. Oldenburg, A.L. James, K. Pruess, and G.J. Moridis, Mathematical modeling of permeation grouting and subsurface barrier performance, in *Proceedings of the International Containment Technology Conference,* pp. 438-444, St. Petersburg, Florida, Feb. 9-12, 1997.

Finsterle, S., G.J. Moridis, and K. Pruess, A TOUGH2 equation-of-state module for the simulation of two-Phase flow of air, water, and a miscible gelling liquid, *Report LBL-36086*, Lawrence Berkeley Laboratory, Berkeley, CA, 1994 (on the web at URL http://www-esd.lbl.gov/ITOUGH2/Bibliography/Abstract/LBL_EosGel.html).

Leverett, M.C., Capillary behavior in porous media, *AIME Trans., 142*, 152-158, 1941.

Moridis, G.J., A. James, and C. Oldenburg, Development of a design package for a viscous barrier at the Savannah River site, *Land Contamination and Reclamation, 5*(3), 149-153, 1997a.

Moridis, G.J., P. Persoff, J. Apps, L. Myer, K. Pruess, and P. Yen, A field test of permeation grouting in heterogeneous soils using a new generation of barrier liquids, in *Barrier Technologies for Environmental Management*, pp. D133-D143, National Academy Press, Washington, D.C., 1997b.

Moridis, G.J., P. Persoff, P. Yen, L. Myer, S. Finsterle, P. Williams, and K. Pruess, A design study for a medium-scale field demonstration of the viscous barrier technology, *Report LBNL-38916*, Lawrence Berkeley National Laboratory, Berkeley, CA, 1996a (on the web at URL http://www-esd.lbl.gov/BarrierStudies/Publications/LBNL38916) .

Moridis, G.J., L. Myer, P. Persoff, S. Finsterle, J.A. Apps, D. Vasco, S. Muller, P. Williams, P. Yen, and K. Pruess, A field test of a waste containment technology using a new generation of injectable barrier liquids, *Report LBNL-38817*, Lawrence Berkeley National Laboratory, Berkeley, CA, 1996b (on the web at URL http://www-esd.lbl.gov/BarrierStudies/Publications/LBNL38817) .

Moridis, G.J., P. Persoff, J. Apps, A. James, C. Oldenburg, A. McGrath, B. Freifeld, L. Myer, L. Pellerin, and K. Pruess, A design study for the isolation of the 281-3H retention basin at the Savannah River site using the viscous barrier technology, *Report LBNL-38920*, Lawrence Berkeley National Laboratory, Berkeley, CA, 1996c (on the web at URL http://www-

esd.lbl.gov/BarrierStudies/Publications/LBNL38920) .

Moridis, G.J., L. Myer, P. Persoff, S. Finsterle, J.A. Apps, D. Vasco, S. Muller, P. Williams, P. Yen, B. Freifeld, and K. Pruess, First-level field demonstration of subsurface barrier technology using viscous liquids, *Report LBL-37520*, Lawrence Berkeley National Laboratory, Berkeley, CA, 1995 (on the web at URL http://www-esd.lbl.gov/BarrierStudies/Publications/LBL37520).

Moridis, G.J., P. Persoff, H.-Y. Holman, S.J. Muller, K. Pruess, and C.J. Radke, New barrier fluids for subsurface containment of contaminant, in *Proceedings of ER93 Environmental Remediation Conference*, pp. 941-948, October 24-28, Augusta, GA, 1994.

MSE Technology Applications, Inc., Viscous liquid barrier cold site demonstration final report, *Report HMP-55*, MSE Technology Applications, Butte, Montana, February 1999.

MSE Technology Applications, Inc., Colloidal silica test barrier design package, *Report HMP-47*, MSE Technology Applications, Butte, Montana, June 1997.

Oldenburg, C.M., and F.J. Spera, Hybrid model for solidification and convection, *Numerical Heat Transfer, Part B, 21*, 217-229, 1992.

Persoff, P., G.J. Moridis, J.A. Apps, and J. Whang, Effect of dilution and contaminants on sand grouted with colloidal silica, *ASCE J. Geotech. Geoenv. Eng., in press*, 1999.

Persoff, P., G.J. Moridis, J.A. Apps, and K. Pruess, Evaluation tests for colloidal silica for use in grouting applications, *ASTM Geotech. Testing J., 21*(3), 264, 1998.

Persoff, P., G.J. Moridis, J. Apps, K. Pruess, and S. Muller, Designing injectable colloidal silica barriers for waste isolation at the Hanford site, *AIChE Symp. Series, 91*, (306), 58-67, 1995.

Persoff, P., S. Finsterle, G.J. Moridis, J. Apps, K. Pruess, and S. Muller, Injectable barriers for waste isolation, in *33rd Hanford Symposium on Health and Environment, In-Situ Remediation:Scientific Basis for Current and Future Technologies, Part 1*, edited by G.W. Gee and N.R. Wing, pp. 87-101, Batelle Press, Columbus, OH, 1994.

Pruess, K., TOUGH2 - A general purpose numerical simulator for multiphase fluid and heat flow, *Report LBL-29400*, Lawrence Berkeley Laboratory, Berkeley, CA, 1991.

Todd, B.J., Numerical modeling of in situ gelation in porous media, Ph.D. dissertation, Dept. of Chem. and Petr. Eng., Univ. of Kansas.

van Genuchten, M.T., A closed-form equation for predicting the hydraulic conductivity of unsaturated soils, *Soil Sci. Soc. Am. J., 44*, 892-898, 1980.

Table 1. Simulation parameters in the primary injections of the OBD

Parameter	Value
$\Delta\ell_1$ (*)	0.15 m
$\Delta\ell_2$ (*)	0.15 m
Lance spacing(+)	1.2 m
Injection spacing(+)	1.4 m
Injection rate (*)	0.5 kg/s
Injected mass (*)	1500 kg of CS+electrolyte/bulb
CS system density	1200 kg/m^3 at $P = 1.013 \times 10^5$ Pa and $T = 15^o$C
γ_1	3.22×10^{-3} Pa·s
γ_2	2.82×10^{-4} Pa·s
γ_3	1.35×10^{-3} 1/s
Mixing rule	Linear [*Finsterle et al.*, 1994]
F	Power-law model [*Todd*, 1990], $\beta = 2$
Gel-time scaling factor (*)	2.0

(*): Parameter to be optimized, (+): Derived parameter

Table 2. Optimized design parameters in the OBD (46 iterations)	
Parameter	**Value**
$\Delta\ell_1$	0.1125 m
$\Delta\ell_2$	0.105 m
Lance spacing	0.9 m
Injection spacing	0.9 m
Injection rate	0.335 kg/s
Injected mass (primary injections)	402 kg of CS+electrolyte/bulb
Gel-time scaling factor	1.6

Table 3. Design parameters in the SED	
Parameter	**Value**
Lance spacing	0.7 m
Injection spacing	0.7 m
Injection rate (primary and secondary)	0.342 kg/s
Injection rate (tertiary)	0.171 kg/s
Injected mass (primary and secondary)	82 kg of CS+electrolyte/bulb
Injected mass (tertiary)	41 kg of CS+electrolyte/bulb
Gel-time scaling factor (primary and secondary)	1.25
Gel-time scaling factor (tertiary)	2.5

Table 4. In situ permeability measurements of the BNL barrier

N_w [D(m)]	K^* (m/s)	N_w [D(m)]	K^* (m/s)	N_w [D(m)]	K^* (m/s)
1-1a [1.2]	4.93×10^{-7}	1-2a [1.2]	1.85×10^{-4}	1-3a [1.2]	1.58×10^{-6}
1-1b [1.2]	3.88×10^{-6}	1-2b [1.2]	3.51×10^{-5}	1-3b [1.2]	1.32×10^{-6}
1-5a [1.2]	2.00×10^{-6}	1-7a [1.2]	4.76×10^{-5}	2-1a [2.7]	3.88×10^{-8}
1-5b [1.2]	1.77×10^{-5}	1-7b @ 1.2	2.75×10^{-5}	2-1b [2.7]	3.83×10^{-6}
2-2a [2.7]	1.68×10^{-2}	2-2a [3]	5.99×10^{-5}	2-2a [3.6]	6.85×10^{-6}
2-2b [2.7]	3.02×10^{-2}	2-2b [3]	1.28×10^{-4}	2-2b [3.6]	4.02×10^{-6}
2-5a [2.7]	4.95×10^{-4}	2-5a [3.6]	1.59×10^{-4}	2-5a [3.9]	6.53×10^{-5}
2-5b [2.7]	8.96×10^{-4}	2-5b [3.6]	5.22×10^{-6}	2-5b [3.9]	9.57×10^{-5}
2-9a [2.1]	2.23×10^{-6}	2-9a [2.4]	9.57×10^{-5}	2-4a [2.7]	3.28×10^{-2}
2-9b [2.1]	2.79×10^{-6}	2-9b [2.4]	8.33×10^{-7}	2-4a [3]	3.51×10^{-5}
2-4a [3.6]	5.00×10^{-6}	2-3a [2.7]	4.92×10^{-2}	2-3a [3.6]	1.01×10^{-6}
2-4b [3.6]	2.59×10^{-6}	2-3a [3]	8.51×10^{-3}	2-3b [3.6]	2.58×10^{-6}
3-2a [4.8]	4.50×10^{-6}	3-3a [4.8]	8.08×10^{-5}	3-4a [3.6]	3.83×10^{-6}
3-2b [4.8]	1.34×10^{-6}	3-3b [4.8]	8.20×10^{-4}	3-4b [3.6]	6.79×10^{-6}
3-6a [4.8]	6.79×10^{-6}	3-7a [4.5]	4.70×10^{-5}	4-1a [6.3]	1.80×10^{-5}
3-6b [4.8]	2.39×10^{-6}	3-7b [4.5]	6.21×10^{-4}	4-1b [6.3]	1.10×10^{-6}
4-3a [6.3]	4.48×10^{-5}	4-8a [6.7]	3.50×10^{-5}	4-1a [6.7]	4.60×10^{-6}
4-3b [6.3]	2.43×10^{-5}	4-8b [6.7]	1.23×10^{-4}	4-1b [6.7]	2.20×10^{-6}
4-6a [6.3]	1.61×10^{-5}	5-7a [7.5]	3.41×10^{-6}	4-1a [6.7]	4.60×10^{-6}
5-1a [7.5]	3.30×10^{-5}	5-7b [7.5]	6.34×10^{-4}	4-1b [6.7]	2.20×10^{-6}
B-1a [1.5]	3.85×10^{-3}	B-2a [3]	5.24×10^{-3}		
B-1b [1.5]	6.17×10^{-3}	B-2b [3]	1.28×10^{-2}		

(a): Guelph permeameter head of 5 cm (b): Guelph permeameter head of 10 cm

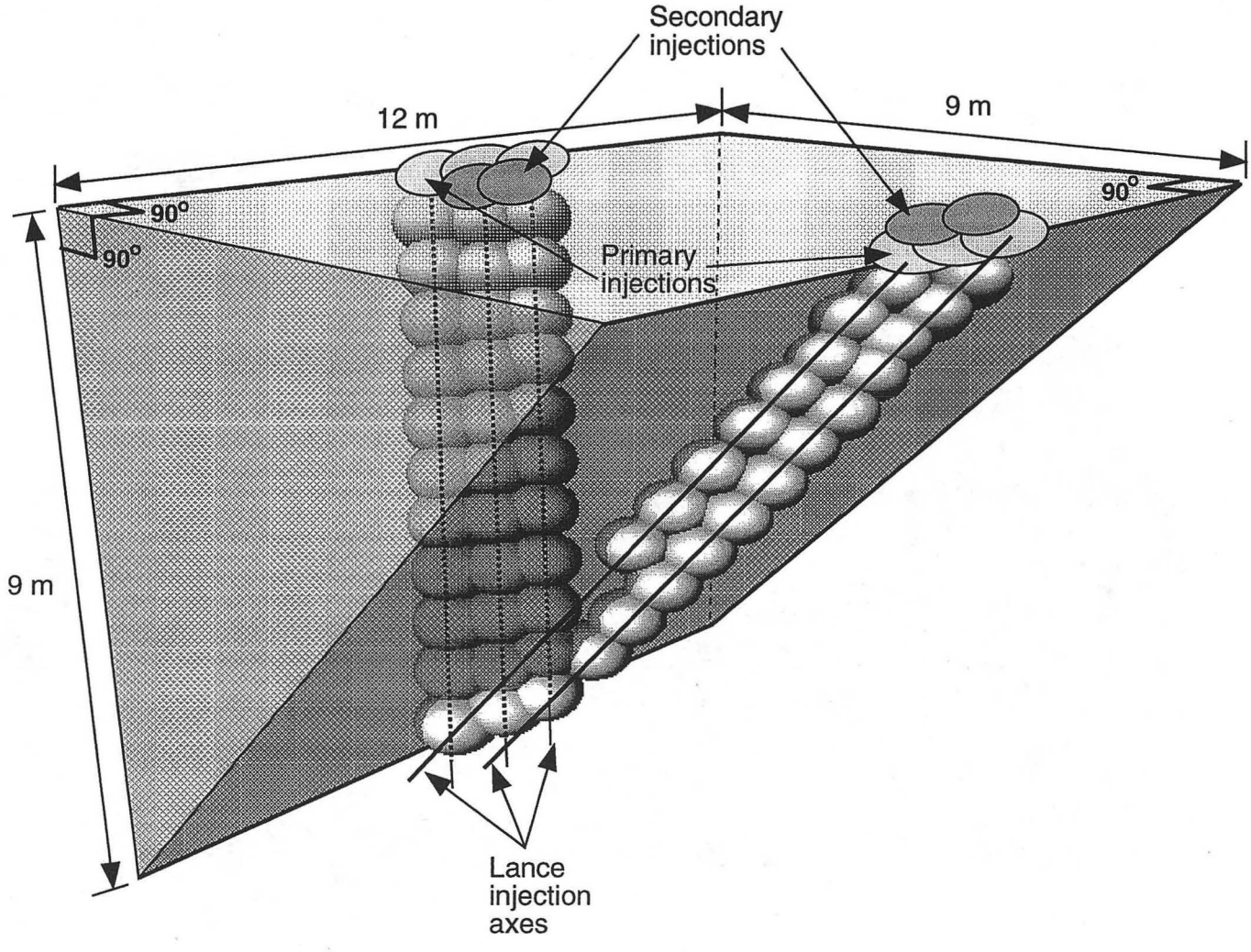

Figure 1. The barrier geometry and dimensions.

Figure 2. The lance injection system used at the BNL site.

Figure 3. Injection holes at the lance tip.

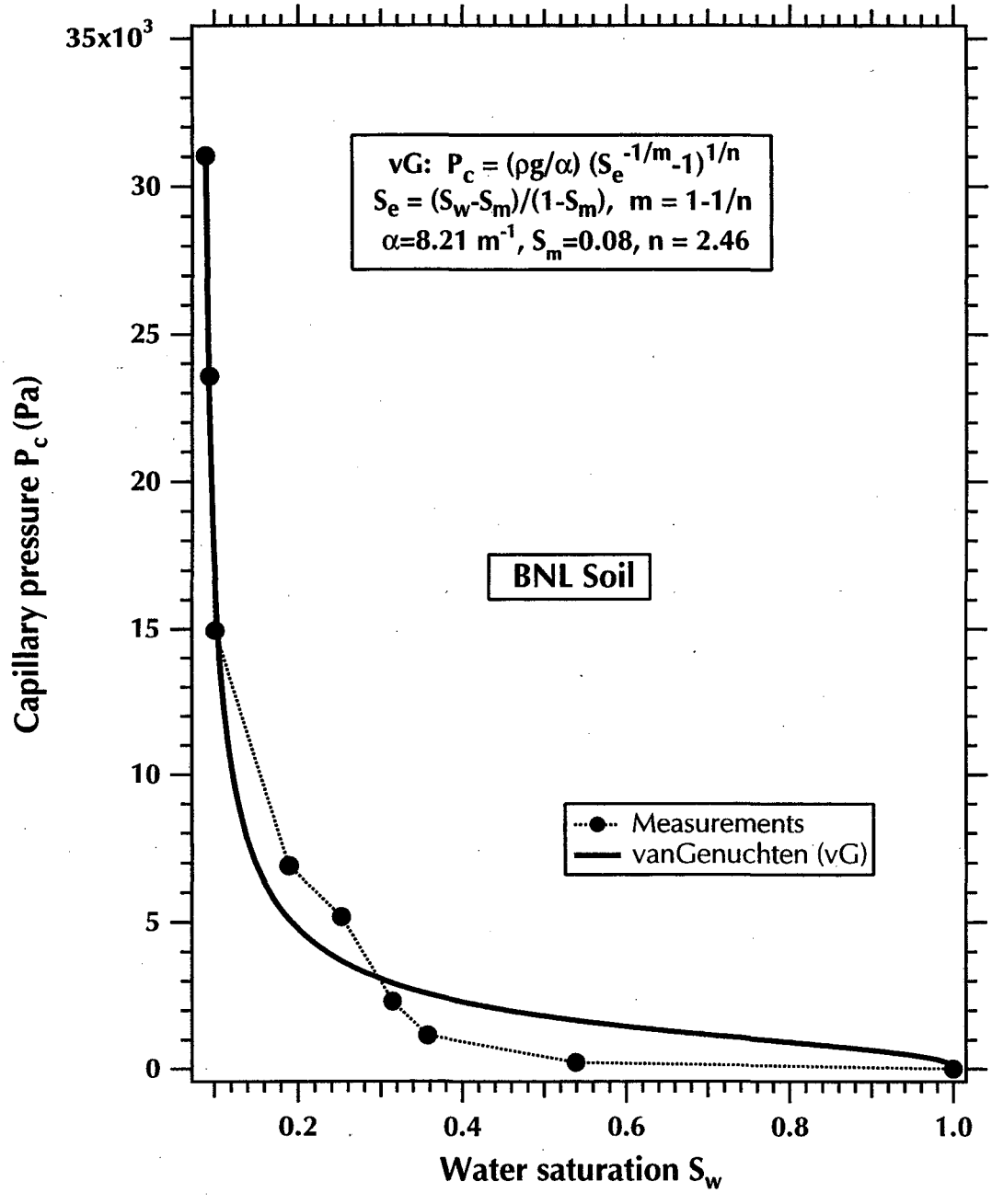

Figure 4. The capillary pressure curve of the BNL soil.

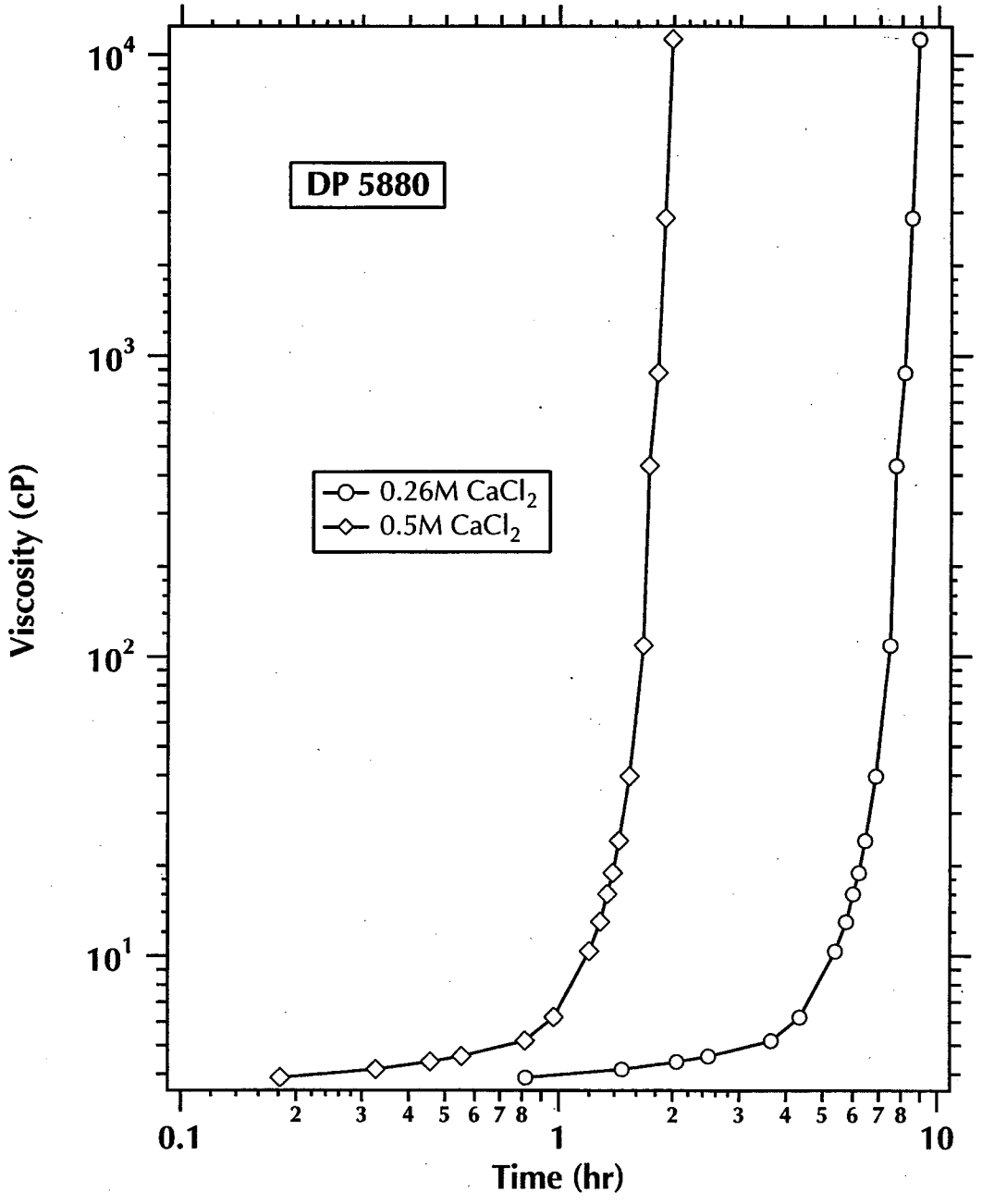

Figure 5. Evolution of viscosity of the DP5880 variant of CS for two concentrations of the gelation-inducing electrolyte (1cp = 0.001 Pa·s).

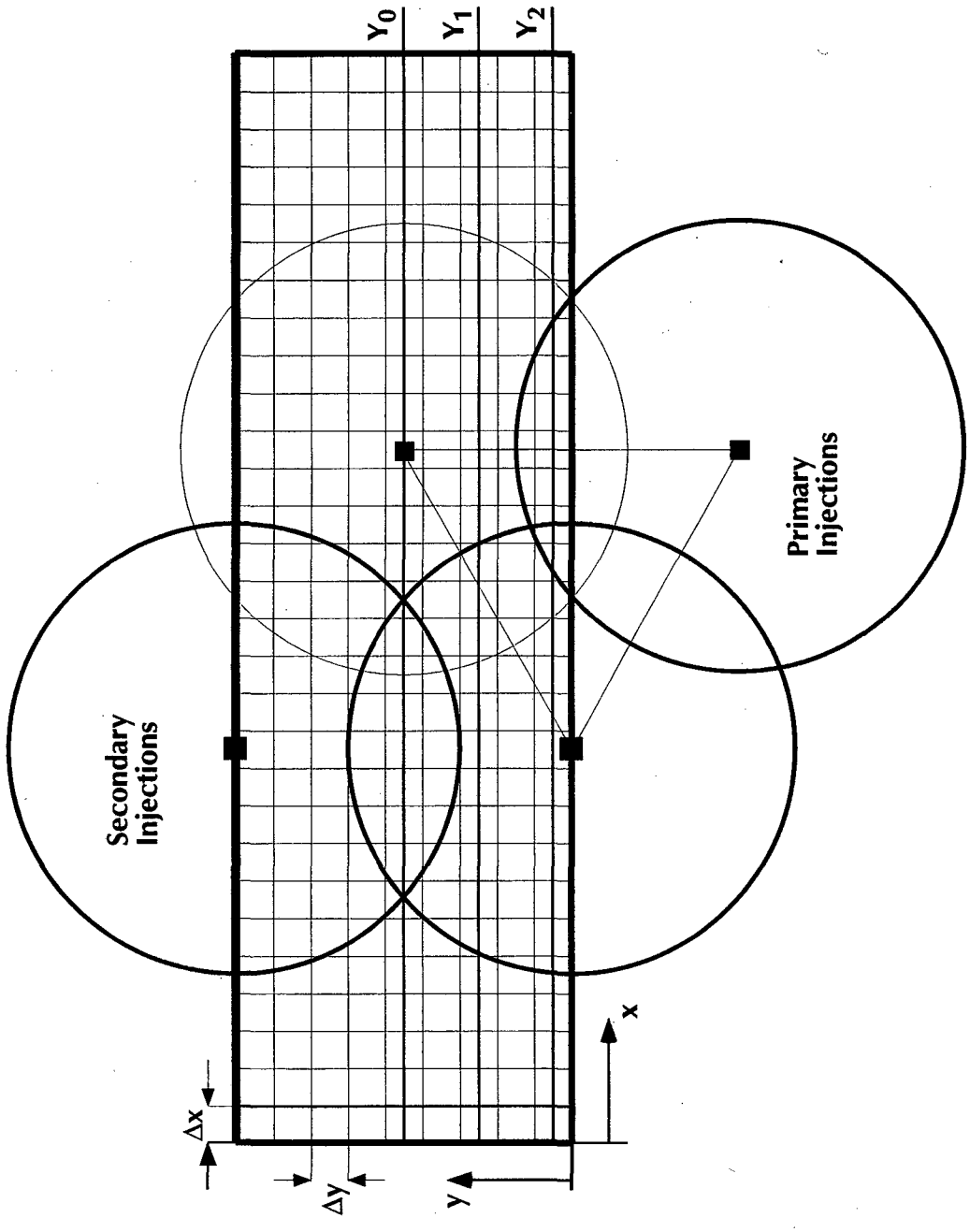

Figure 6. Discretization of the OBD simulation stencil on the (x, y) plane.

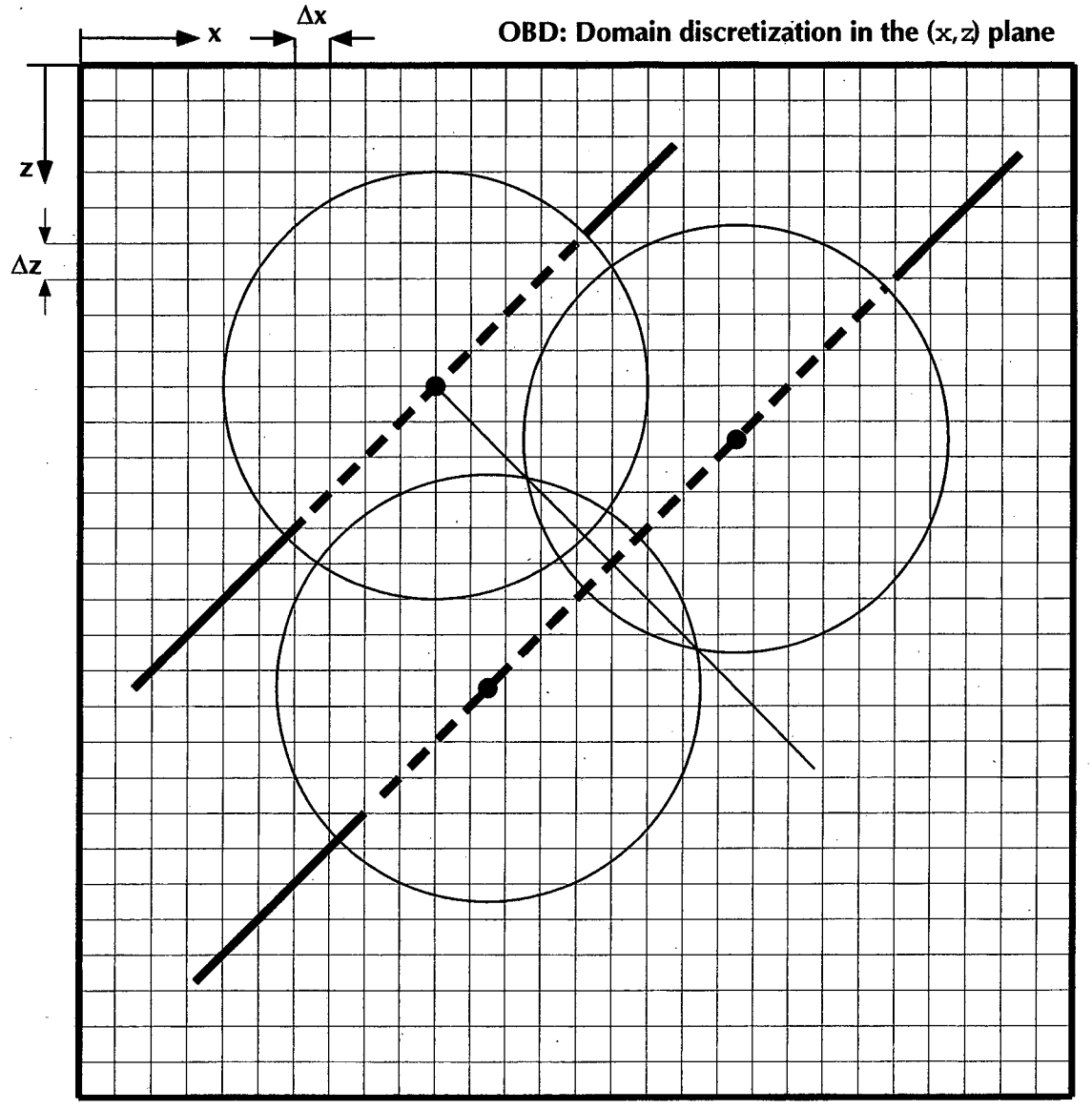

Figure 7. Discretization of the OBD simulation stencil on the (x, z) plane.

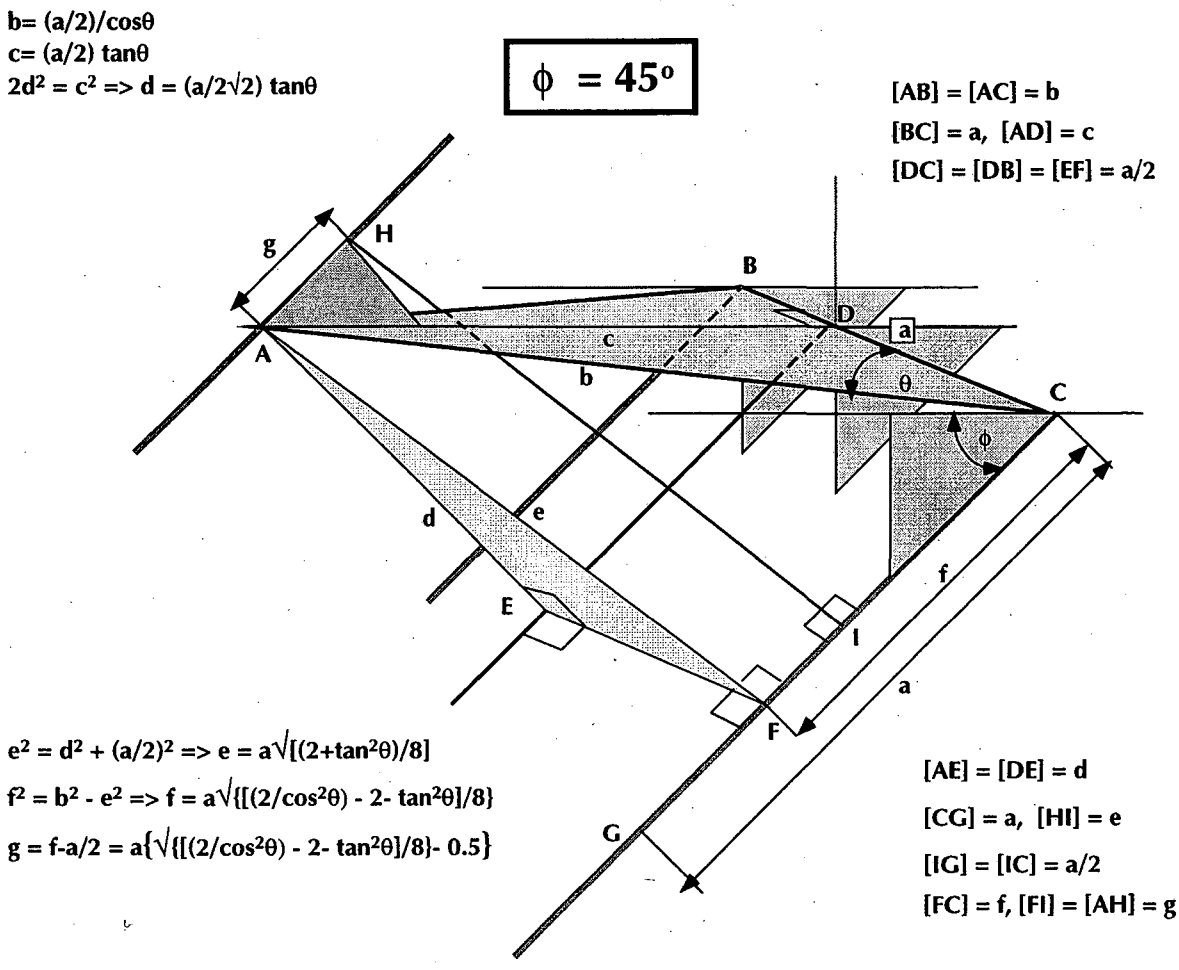

Figure 8. Determination of secondary injection points.

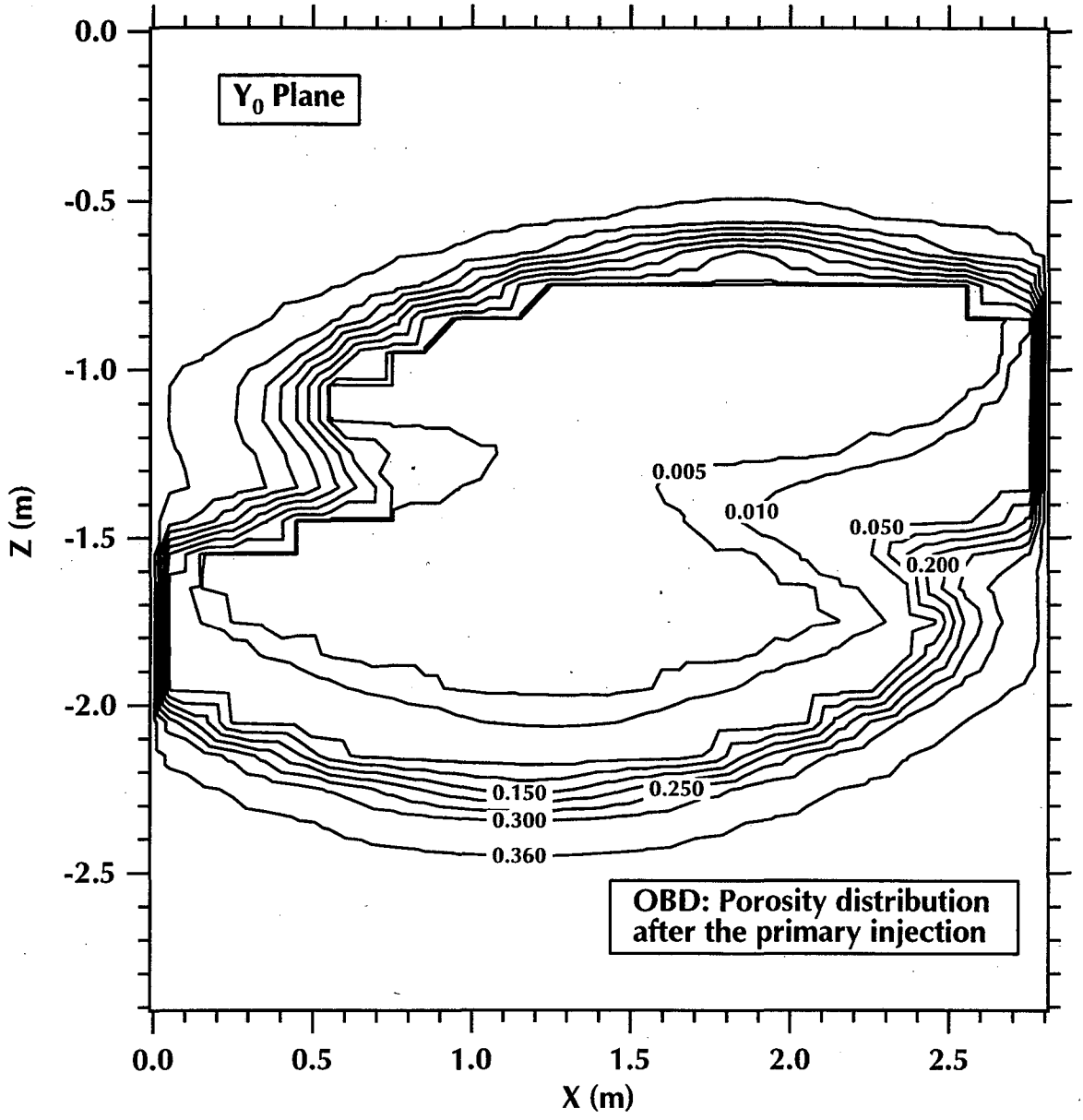

Figure 9. Distribution of ϕ^* on the Y_0 plane after the gelation of the primary injection.

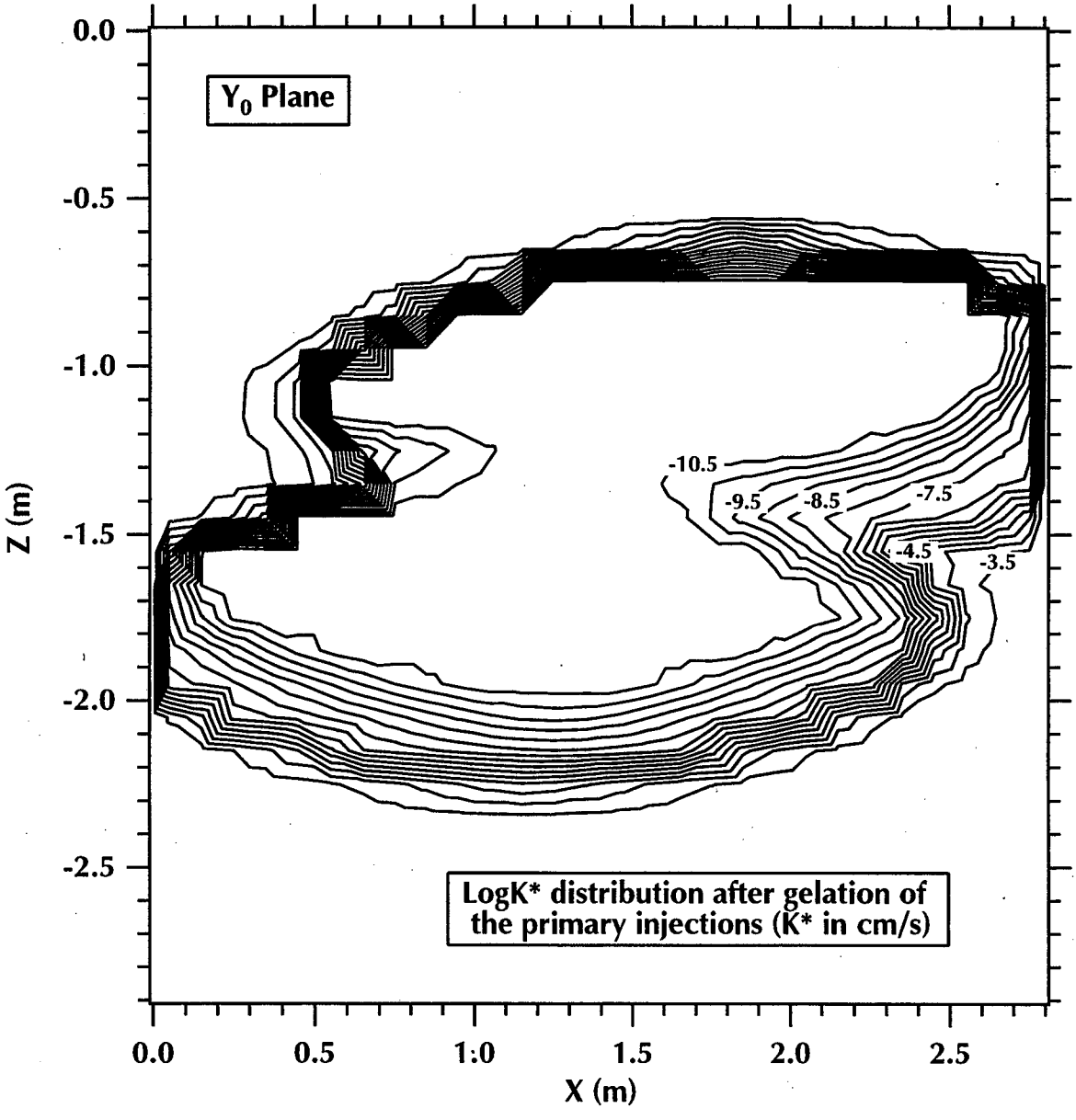

Figure 10. Distribution of $\log(K^*)$ on the Y_0 plane after the gelation of the primary injection in the OBD. The contour interval is 0.5.

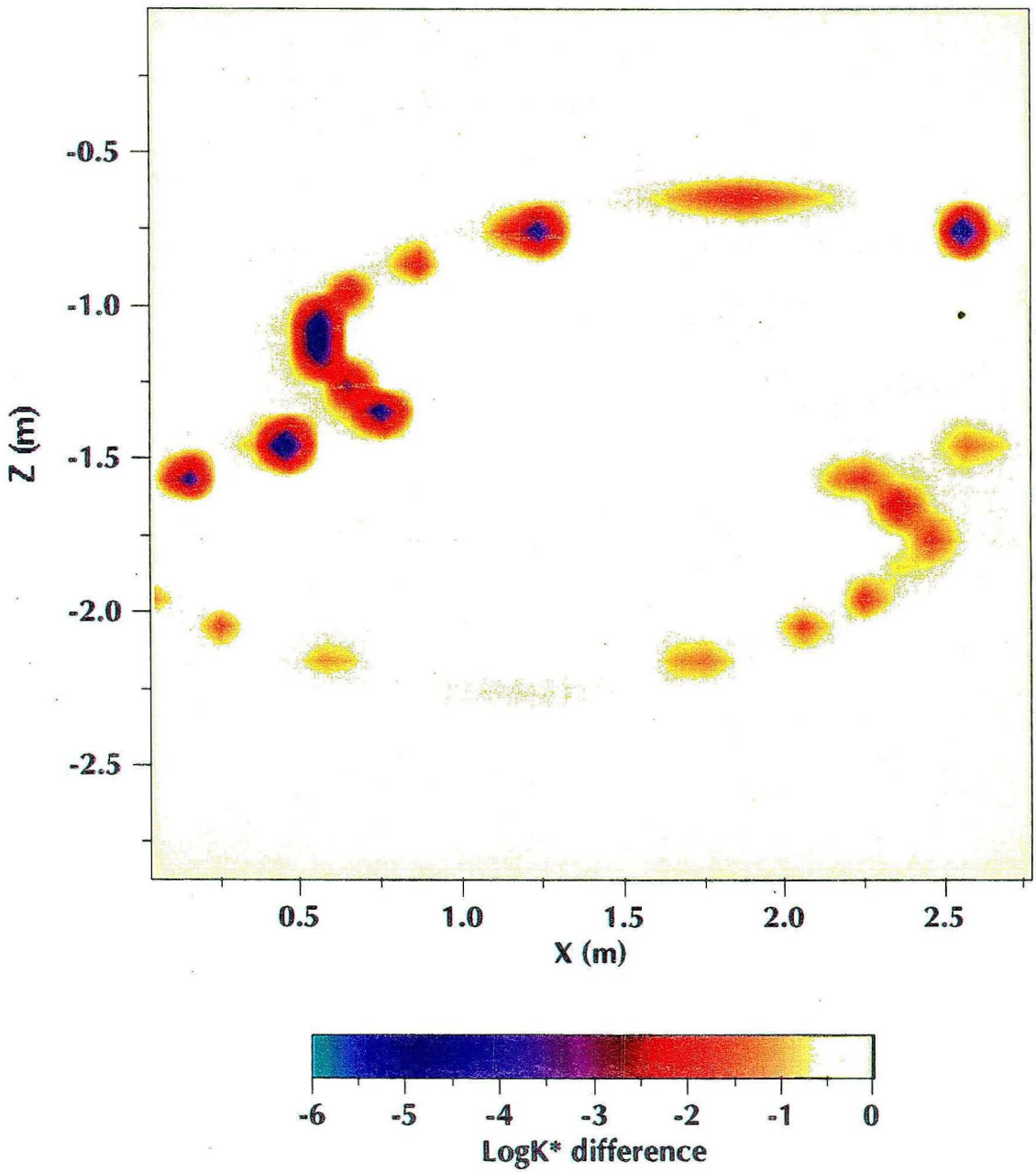

Figure 11. Difference between the distribution of $\log K^*$ on the Y_0 and Y_2 planes after the gelation of the primary injection in the OBD.

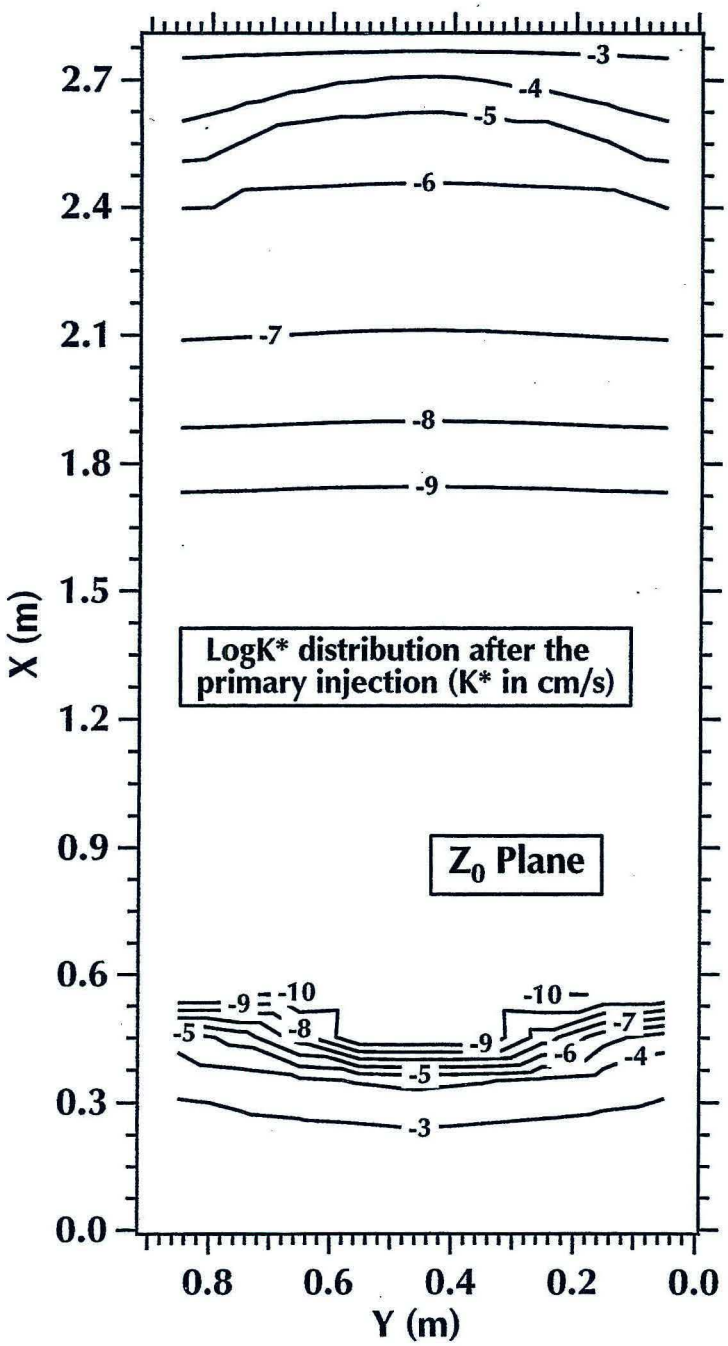

Figure 12. Distribution of $\log K^*$ on the Z_0 plane after the gelation of the primary injection in the OBD. The contour interval is 1.

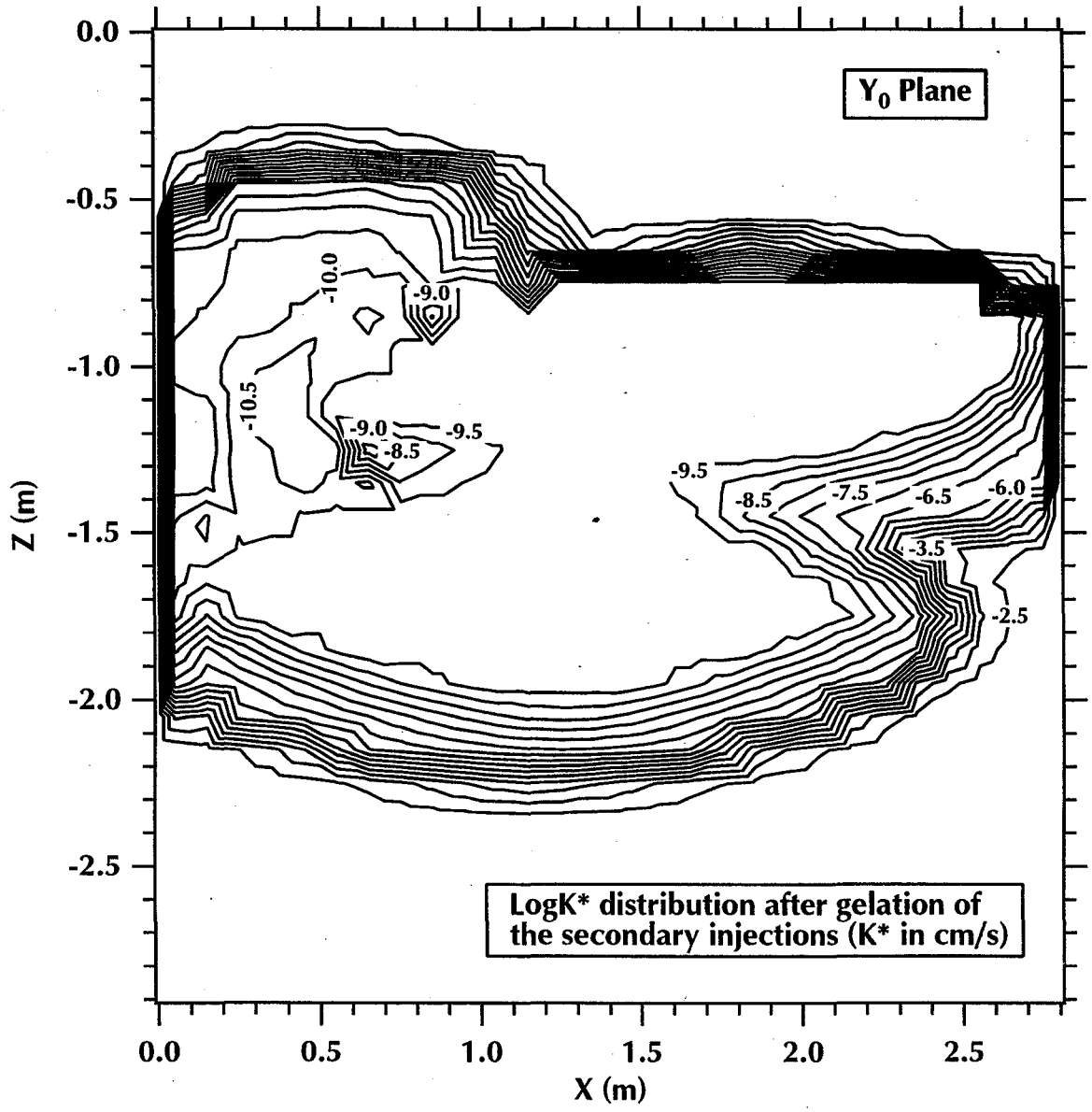

Figure 13. Distribution of $\log K^*$ on the Y_0 plane after the gelation of the secondary injection in the OBD. The contour interval is 0.5.

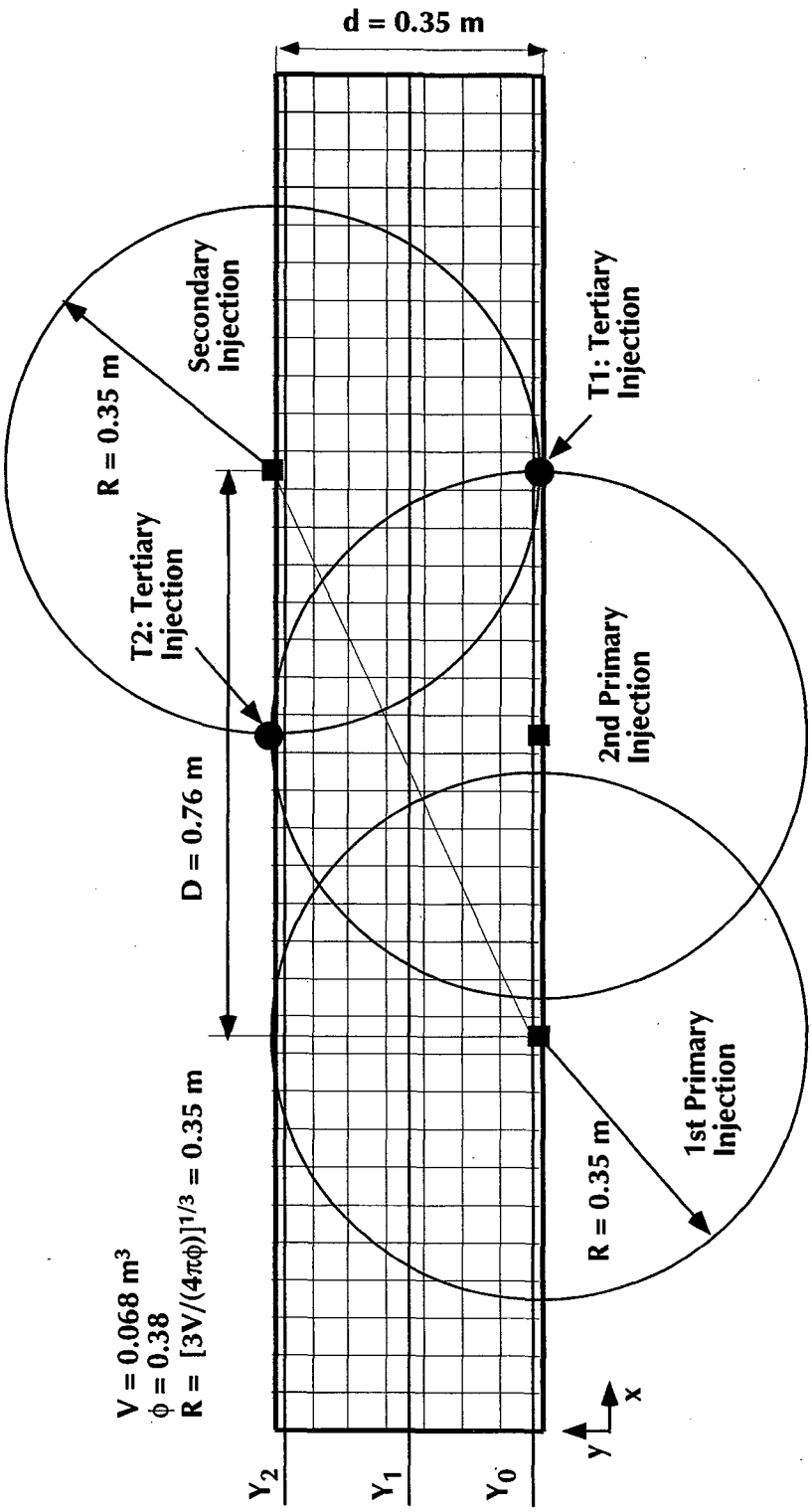

Figure 14. Discretization of the SED simulation stencil on the (x, y) plane.

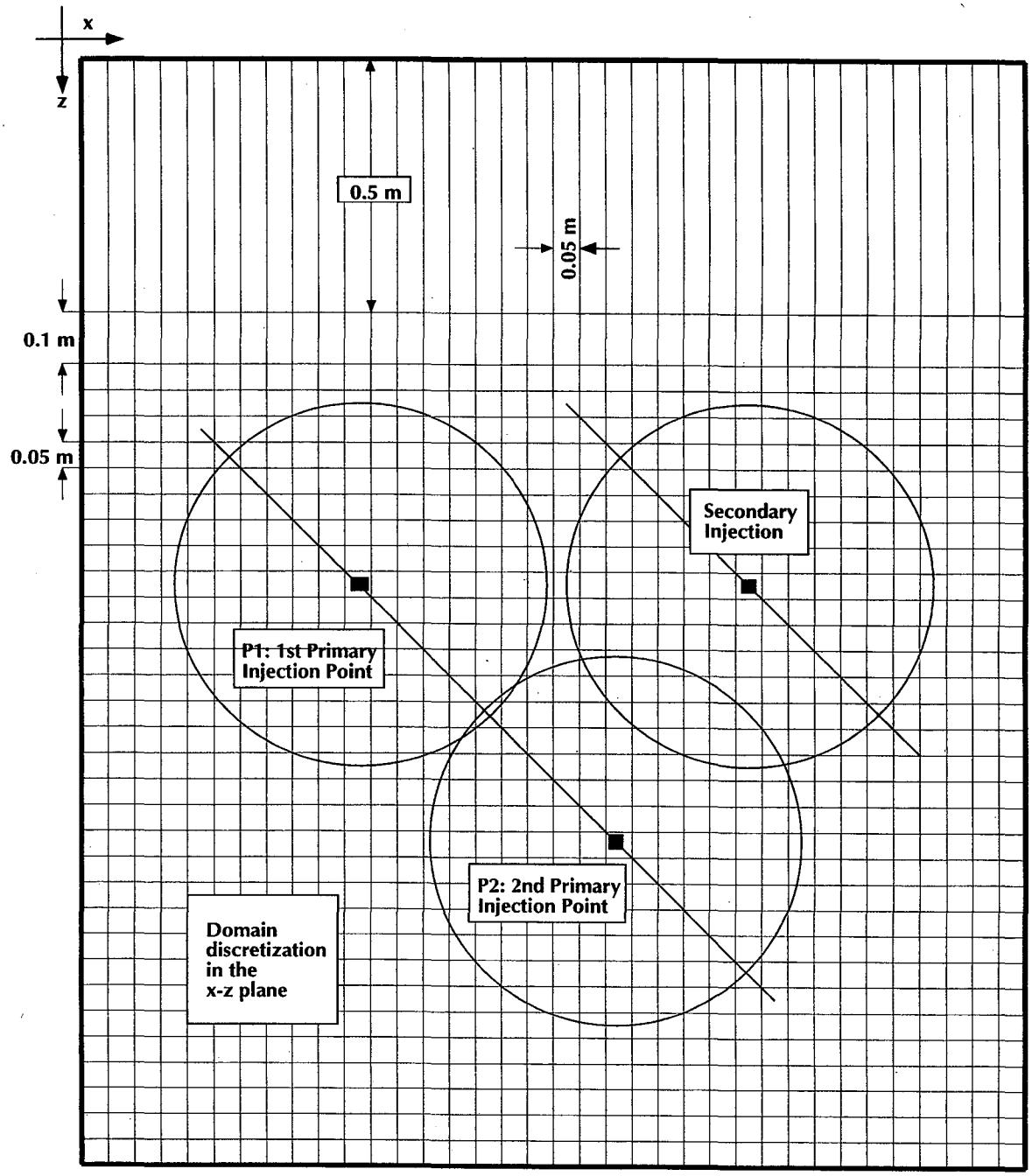

Figure 15. Discretization of the SED simulation stencil on the (x, z) plane.

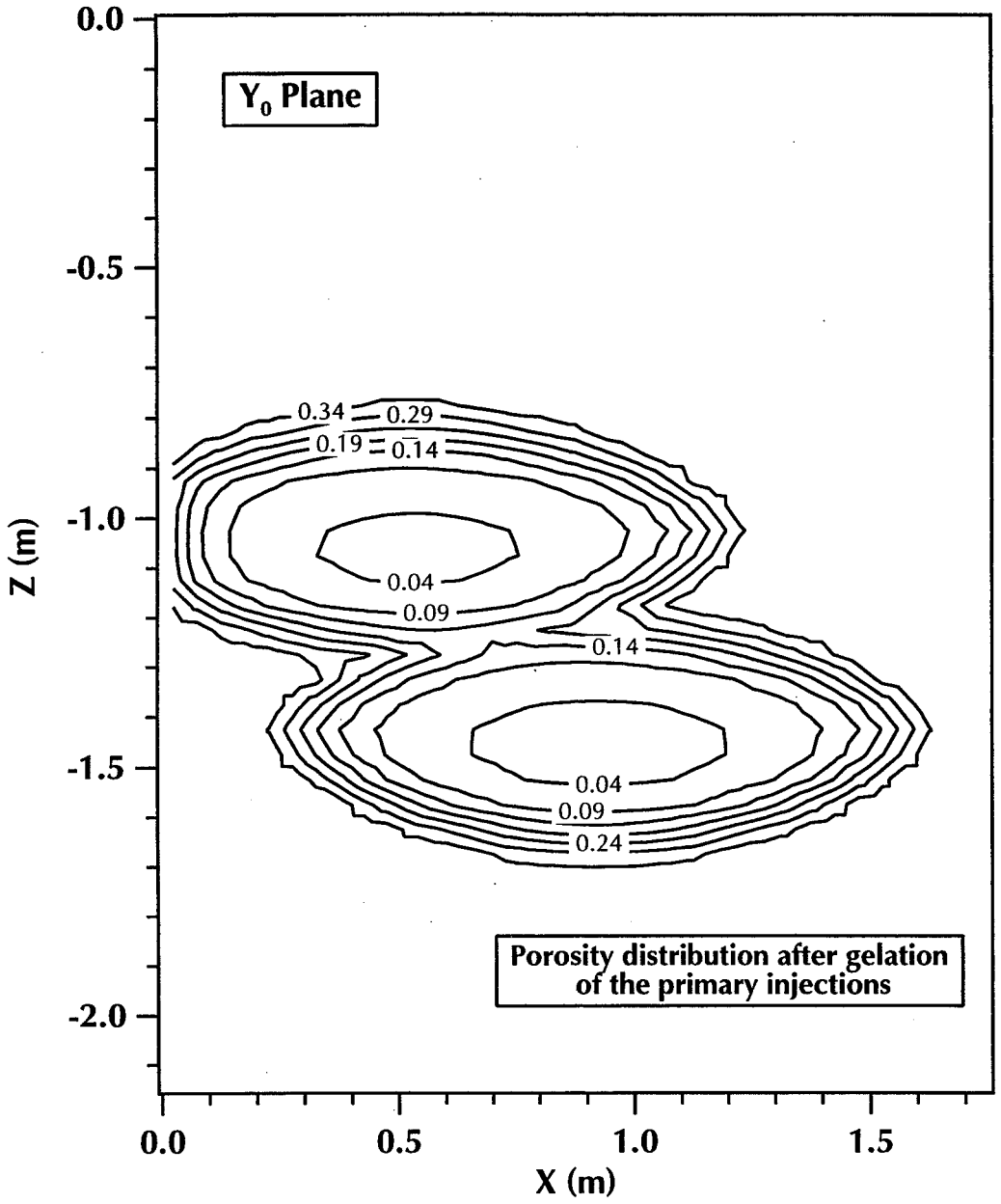

Figure 16. Distribution of ϕ^* on the Y_0 plane after the gelation of the primary injection in the SED. The contour interval is 0.05.

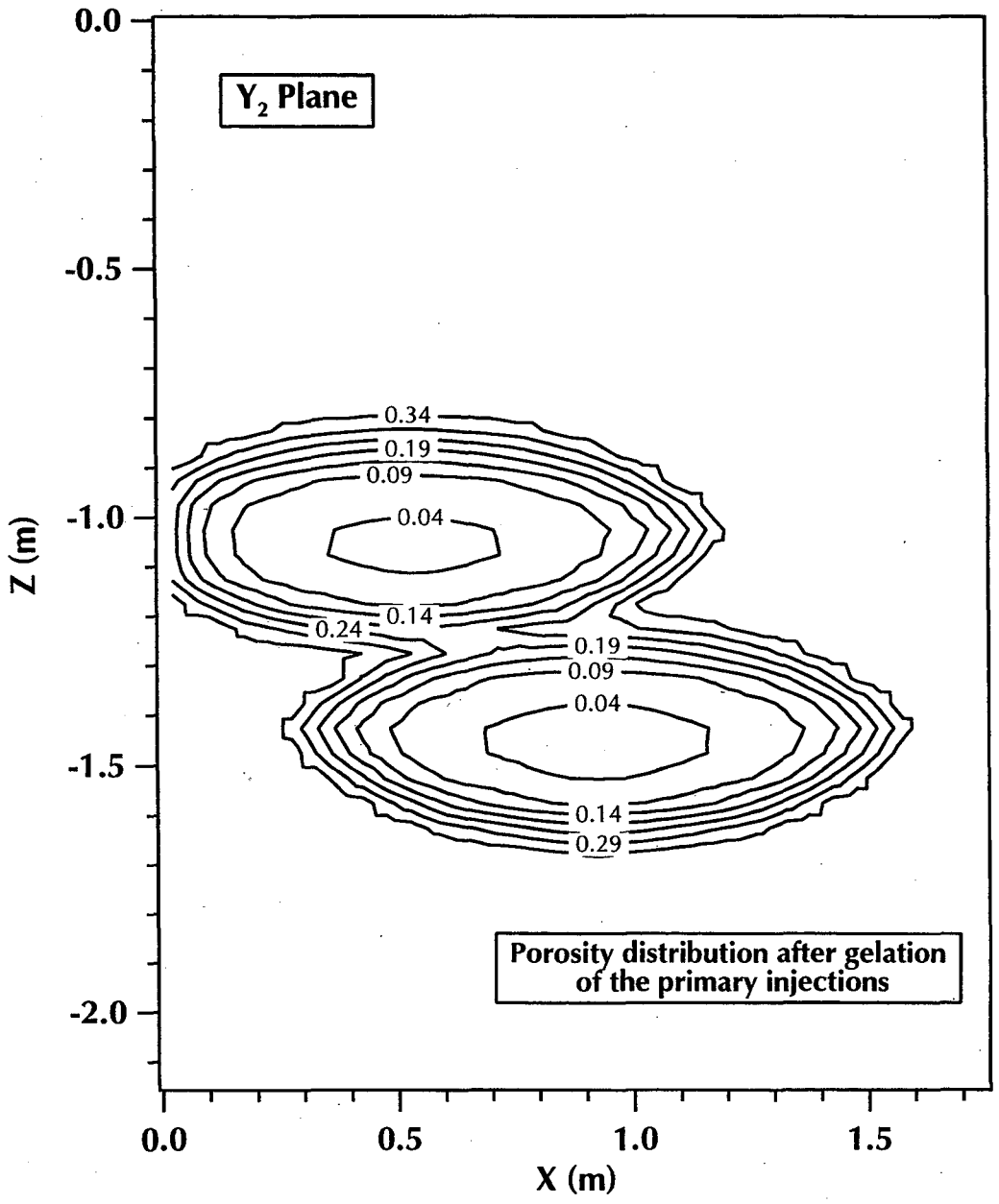

Figure 17. Distribution of ϕ^* on the Y_2 plane after the gelation of the primary injection in the SED. The contour interval is 0.05.

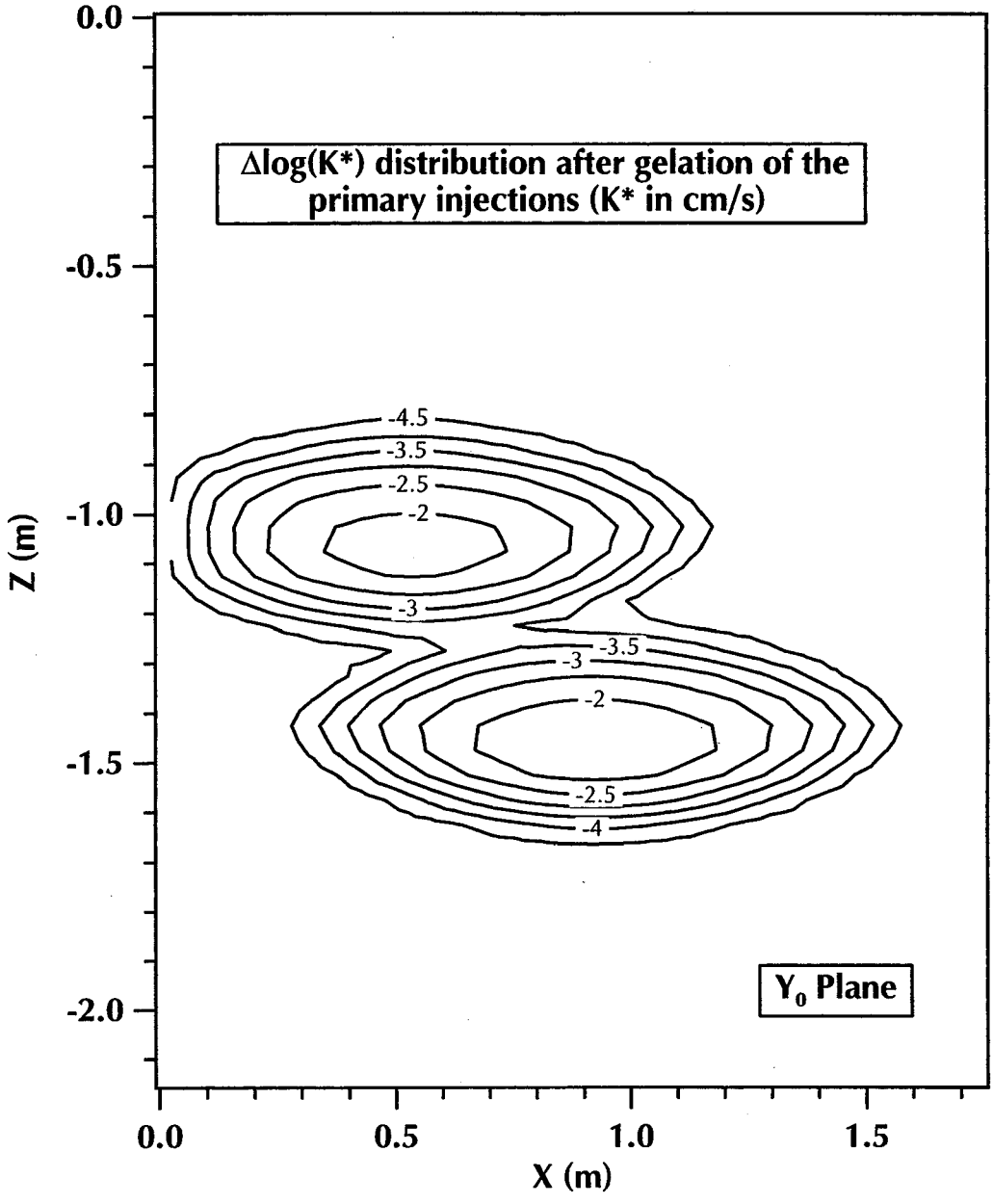

Figure 18. Distribution of $\Delta\log(K^*)$ on the Y_0 plane after the gelation of the primary injection in the SED.

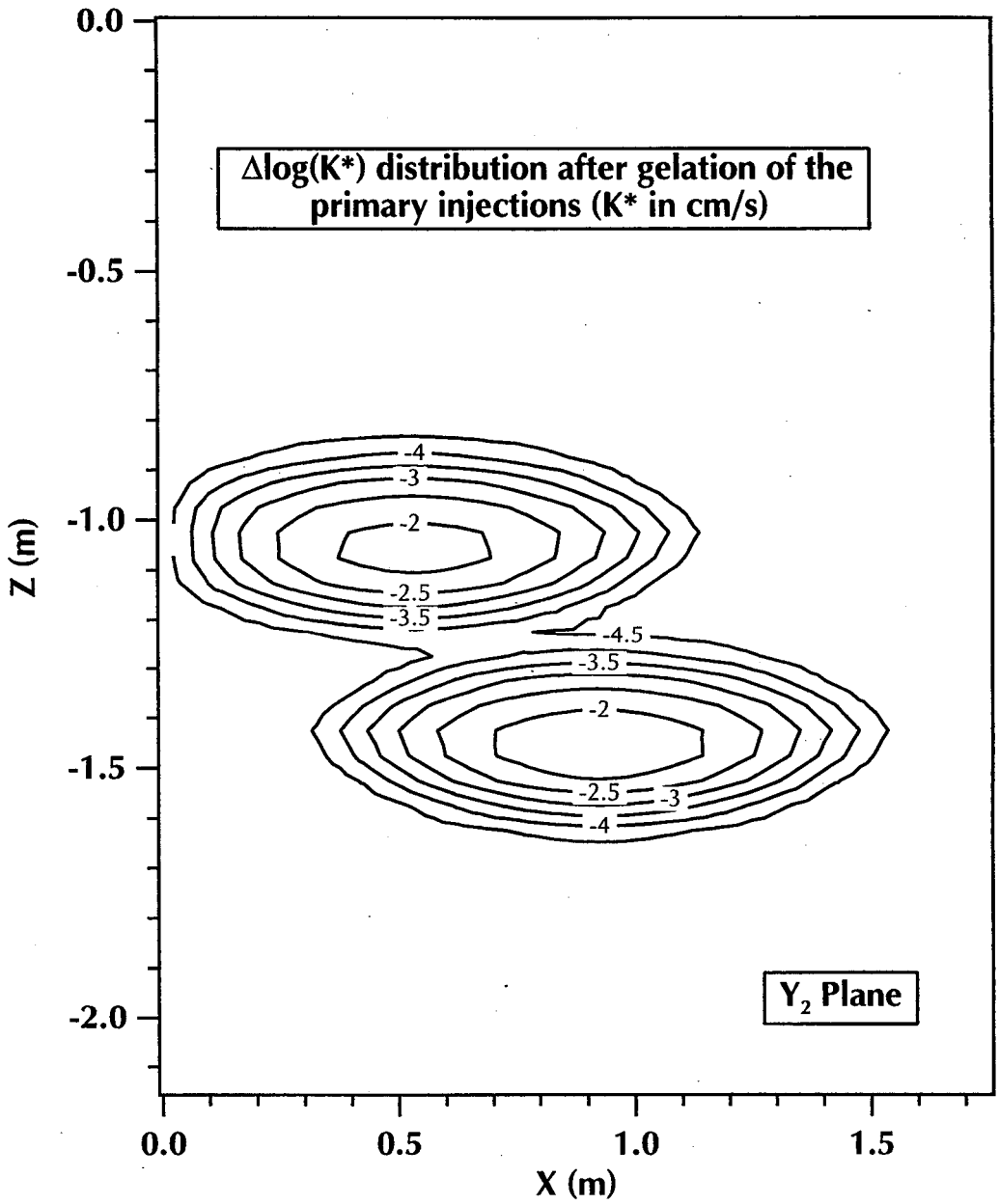

Figure 19. Distribution of $\Delta\log(K^*)$ on the Y_2 plane after the gelation of the primary injection in the SED.

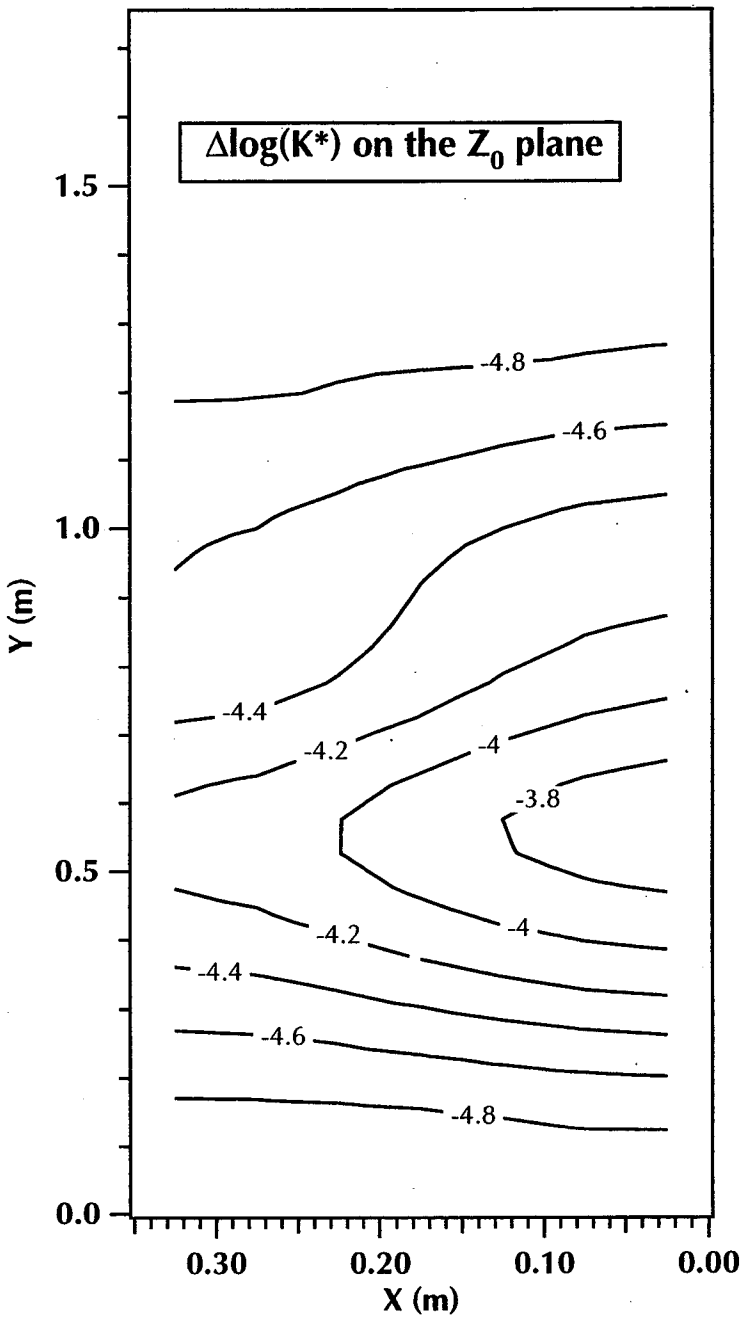

Figure 20. Distribution of $\Delta\log(K^*)$ on the Z_0 plane after the gelation of the primary injection in the SED (K^* in cm/s).

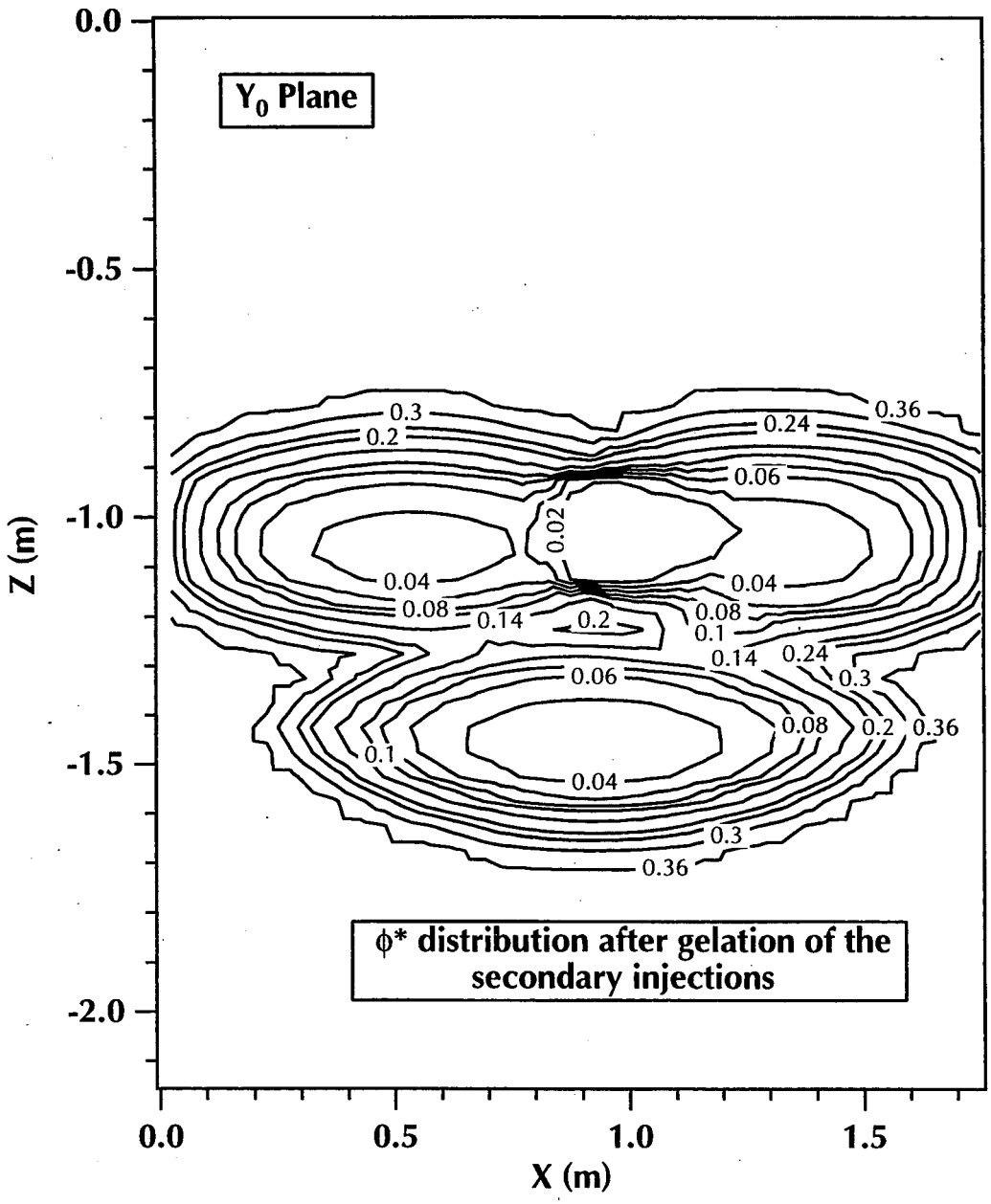

Figure 21. Distribution of ϕ^* on the Y_0 plane after the gelation of the secondary injection in the SED (contours at 0.04, 0.06, 0.08, 0.1, 0.14, 0.2, 0.24, 0.3 and 0.36).

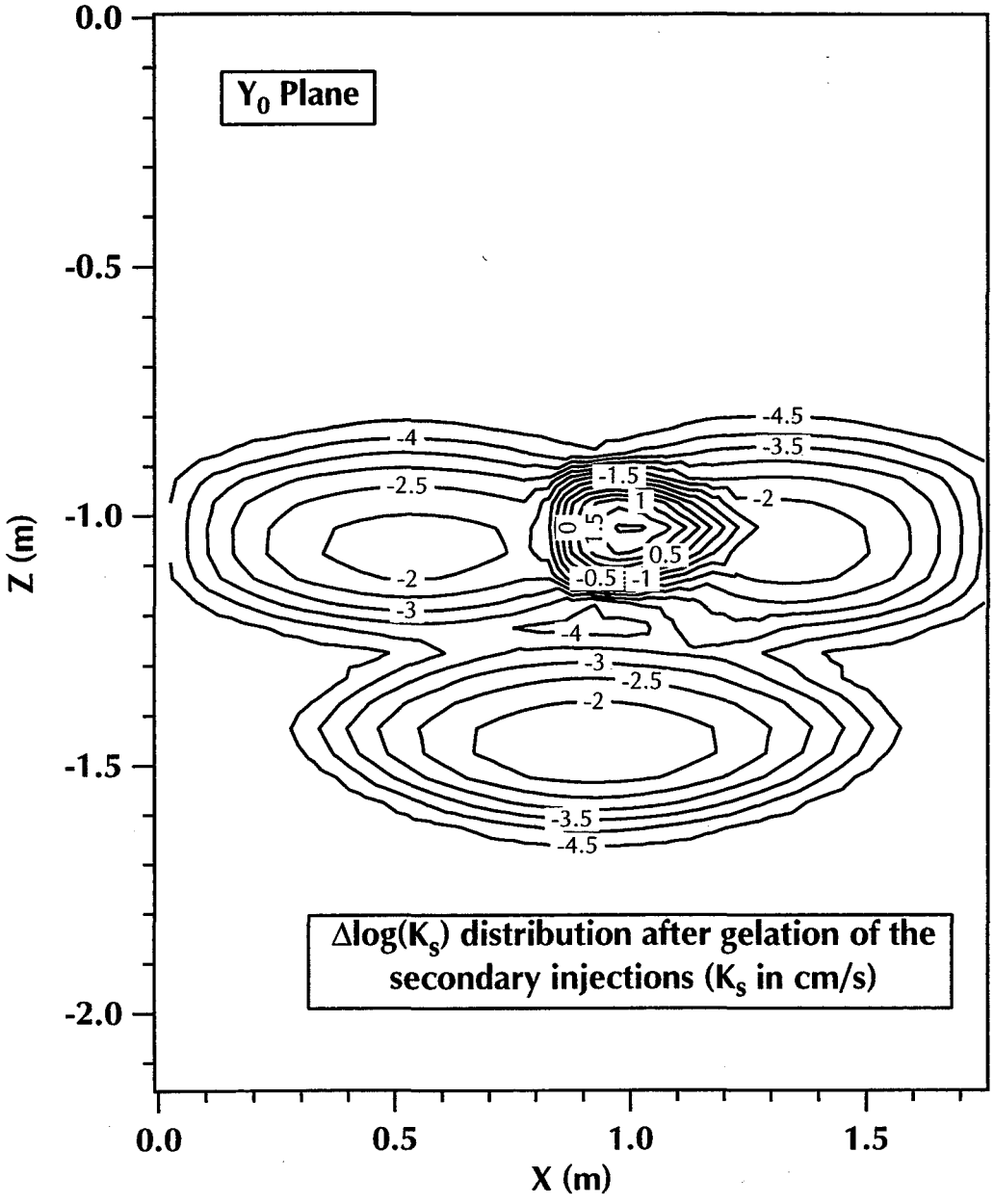

Figure 22. Distribution of $\Delta\log(K^*)$ on the Y_0 plane after the gelation of the secondary injection in the SED. The contour interval is 0.5.

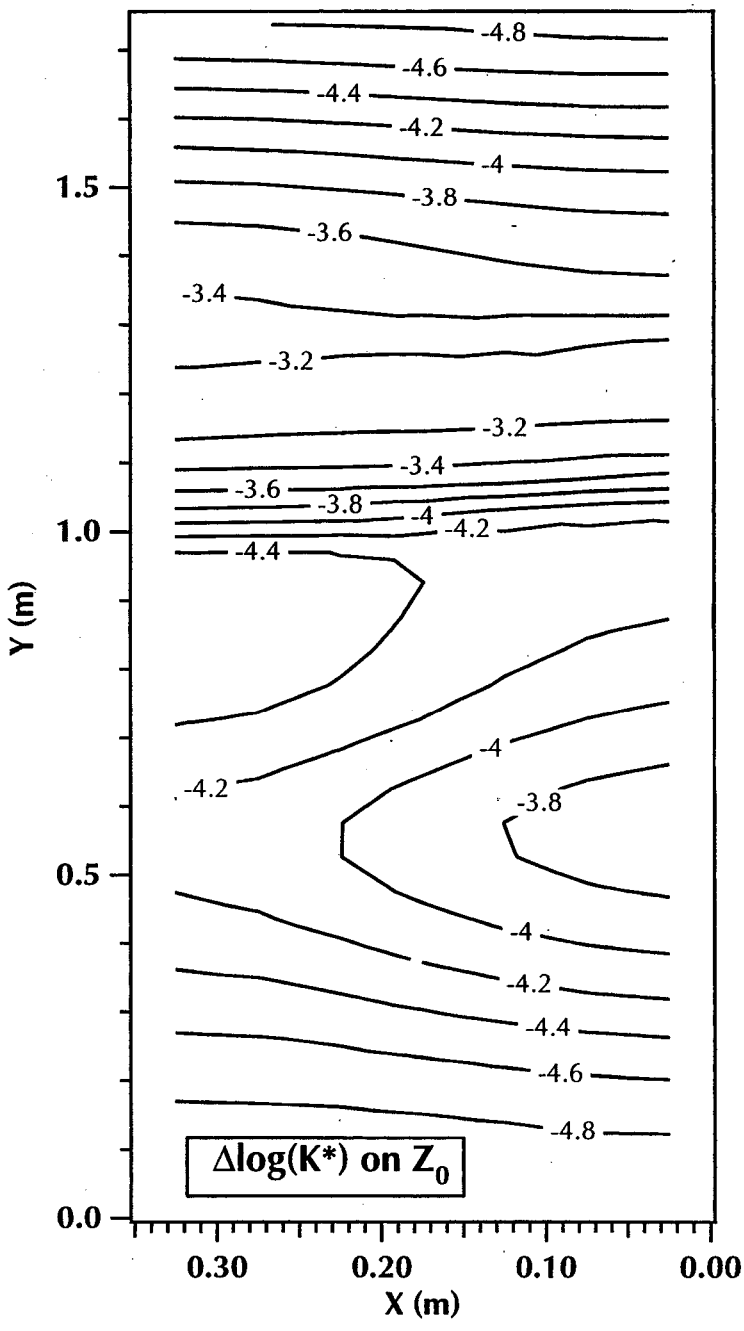

Figure 23. Distribution of $\Delta\log(K^*)$ on the Z_0 plane after the gelation of the secondary injection in the SED.

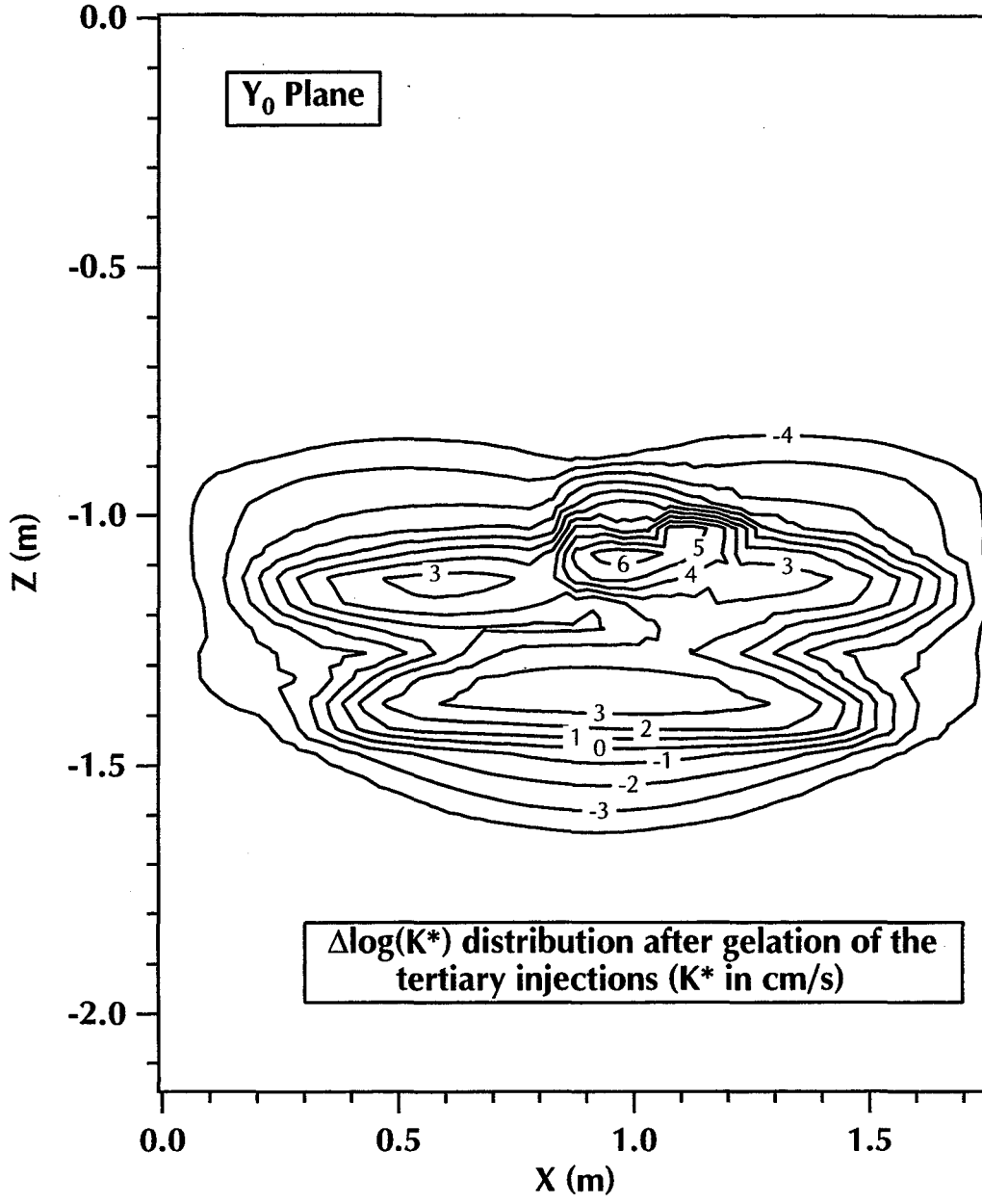

Figure 24. Distribution of $\Delta\log(K^*)$ on the Y_0 plane after the gelation of the secondary injection in the SED.

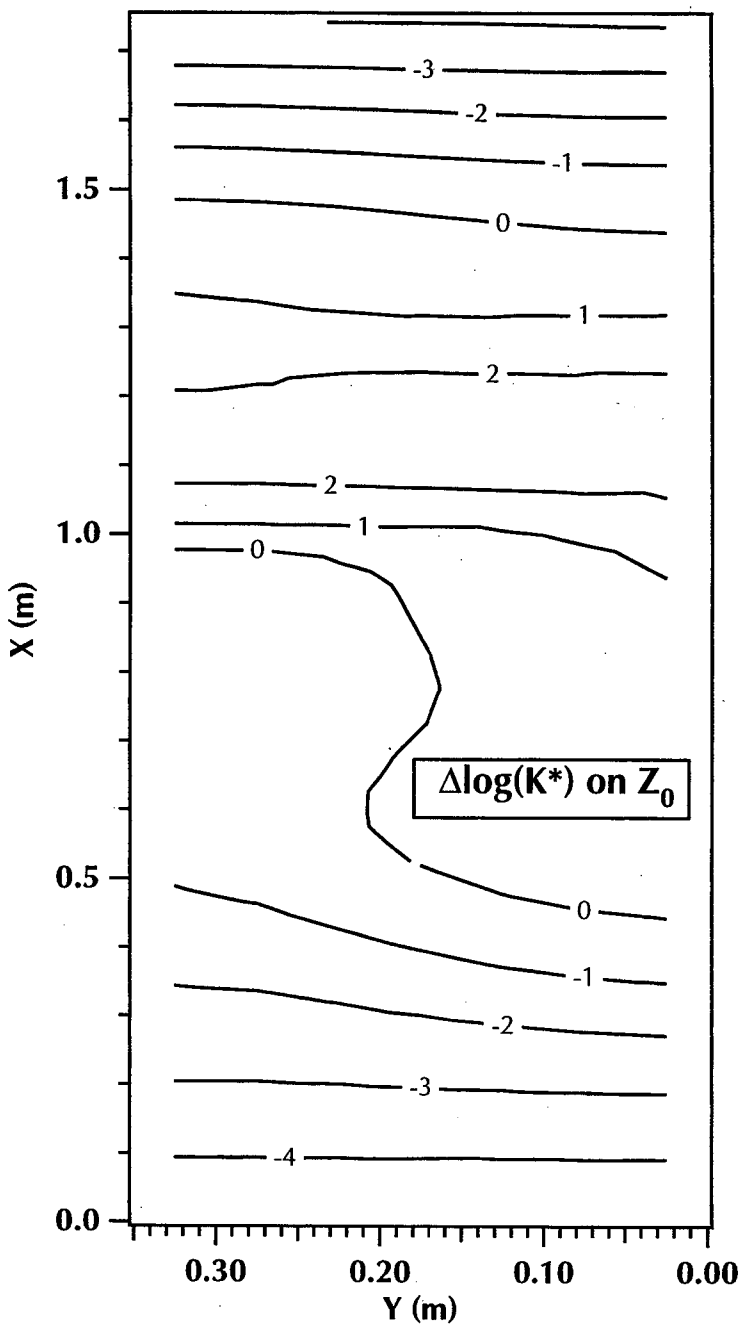

Figure 25. Distribution of $\Delta\log(K^*)$ on the Z_0 plane after the solidification of the tertiary injection in the SED.

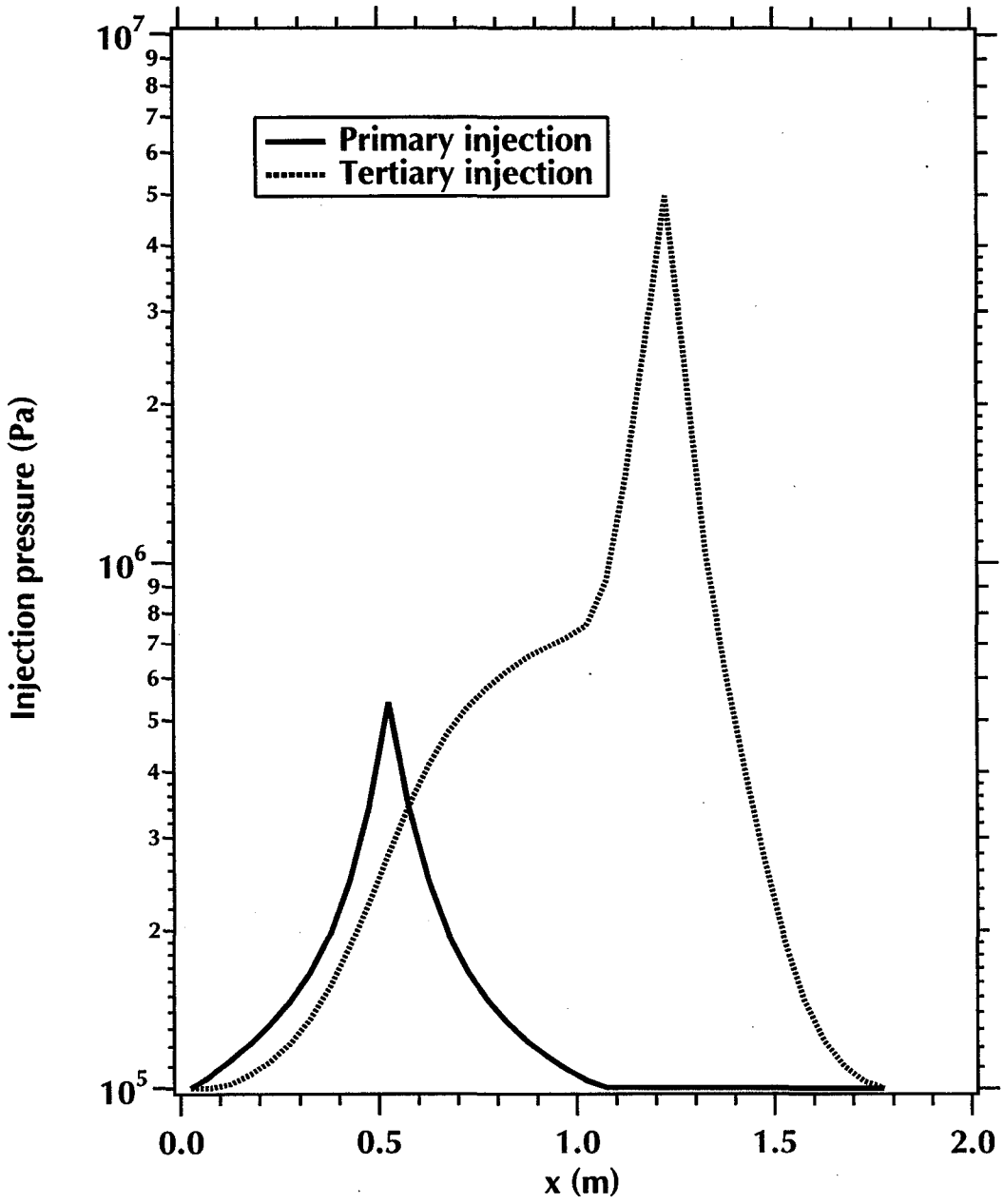

Figure 26. Injection pressure distribution at the end of the primary and tertiary injections (points P1 and T1, respectively) along the x axis passing by the injection points.

Ernest Orlando Lawrence Berkeley National Laboratory
One Cyclotron Road | Berkeley, California 94720

Prepared for the U.S. Department of Energy under Contract No. DE-AC03-76SF00098